IMA Journal of Applied Mathematics (2005) 1−31
doi: 10.1093/imamat/dri017

Linear wave forcing of an array of axisymmetric ice floes

LUKE G. BENNETTS & VERNON A. SQUIRE
Department of Mathematics and Statistics, University of Otago, P.O. Box 56, Dunedin, 9054, New Zealand.

Division of Sciences, University of Otago, Dunedin, New Zealand.

[April 8, 2009]

Under linear and time-harmonic conditions, a set of periodic Green's functions is derived to combine the interactions of an infinite number of identical, equispaced floating bodies. The bodies themselves are compliant, thin-elastic plates that can represent ice floes, and, unlike previous studies they are permitted to vary axisymmetrically in thickness through both their upper and lower surfaces, with a realistic draught also admitted. Initially, the governing equations are simplified by means of an expansion of the vertical dependence of the unknown velocity potential combined with a variational principle, which reduces calculations to the horizontal plane alone. The unknowns of the resulting equations are written as an integral representation in the free-surface domain and as a Fourier expansion in the domain of the ice-covered fluid, and these are matched at their common boundary to complete the solution process. Our method is validated using numerical results for example problems and the effects of varying the distance between the floes, as well as the introduction of thickness variations and submergence, are also demonstrated.

Keywords:
Green's function, periodic array, sea-ice, flexural-gravity waves, scattering

1. Introduction

In recent years a large number of mathematical models have been devised for wave scattering by floating elastic plates, driven in part by a desire to understand how ocean waves couple to sea-ice in the marginal ice zones (MIZs) that skirt the polar regions. MIZs occur in the vicinity of open ocean activity, normally on a seasonal basis when the surface layer of the sea freezes over to create a covering of ice that is relatively thin in comparison to its horizontal dimensions. They are typically very energetic regions affected by strong winds, local currents and wave-induced fluid motions that cause the sea-ice to oscillate to-and-fro and up-and-down, to flex rhythmically and potentially to break up. The small-scale flexural perturbations in the fluid-ice interface are known as flexural-gravity waves because dispersion is affected by both the mechanical bending of the ice and fluid inertia. Due to the dimensions of the sea-ice it is common practice to consider flexural motion as the dominant factor controlling the flux of wave energy through the MIZ and to model this material by means of thin-plate theory (see Timoshenko and Woinowsky-Krieger, 1959).

With the behaviour of the sea-ice expressed via a thin-elastic plate equation, its influence in the mathematical model is that of a sixth-order condition at the fluid surface. The complexity presented by this high-order boundary-condition often leads to unrealistic assumptions about the ice-covering in order to facilitate the solution process. Sea-ice is a naturally heterogeneous material, with irregular shapes, and abundant imperfections such as pressure ridges and cracks, and these features all provide extra sources of scattering that affect the transfer of wave energy through the MIZ. In a quest to better represent the

inhomogeneous properties of sea-ice, sophisticated mathematical methods have been sought: the recent advances in the field are summarised in Squire (2007).

A common simplifying assumption is that ice-coverings are of a uniform thickness and float unrealistically on the fluid surface, that is they have zero draught. However, by extending the single-mode approximation of Porter and Porter (2004), Bennetts et al. (2007) have presented a method for solving problems in which the ice is permitted to vary in thickness and possess an Archimedean draught. This was achieved by defining a multi-mode approximation (MMA), formed by recasting the governing equations as a variational principle and associating the unknown vertical motion with the single-mode that supports propagating waves and a finite number of the modes that support evanescent waves. The MMA is then calculated from a set of equations that exist in the horizontal plane only and will give the full-linear solution to any degree of accuracy by taking a sufficient number of vertical modes. Using the MMA, numerical solutions for ice of varying thickness and a non-zero draught were made for two-dimensional models (Bennetts, 2007; Bennetts et al., 2007, 2009a) and for solitary axisymmetric floes (Bennetts, 2007; Bennetts et al., 2009b).

Particularly in the Arctic Basin and Southern Ocean, the outer parts of the MIZ are composed of aggregations of individual ice floes in addition to sheets of quasi-continuous ice-cover. The individual floes may form in-situ from the freezing of sea-water or they may have broken away from the edge of larger ice sheets, induced by the strains imposed by the passing ocean wave train. When a large number of floes break-away in such a manner, they will serve as a barrier to the interior ice sheet from ocean waves. Here, there is both a response of each individual floe to incoming waves, as well as a response of the ice field as an entity in which the influence of the floes upon each another must be considered. It is this scenario that motivates our work here, and, although our straight-line array is highly idealised, we note that 'bands' of individual floes and ice cakes have been reported to detach from MIZs to create dissociated belts off the ice edge (see Bauer and Martin, 1980). Furthermore, our solution method is designed specifically so that it leads naturally to the solution for multiple lines of ice floes, which is the subject of future work.

We wish to use an as up-to-date model of the floes as possible and for this reason we incorporate the work of Bennetts et al. (2009b), which accounts for varying thickness and an Archimedean draught. However, other noteworthy three-dimensional models exist. For instance, Meylan and Squire (1996), Peter et al. (2004) and Andrianov and Hermans (2005) all give solutions for circular floes of uniform thickness and a zero draught. Meylan (2002) also treats the problem of a solitary floe of uniform thickness and a zero draught but, through numerical evaluation of the *in vacuo* (dry) modes of the plate, gains solutions for floes of a more general shape. Future work will allow us to extend the methods presented in this work to remove the restraint of axisymmetry and to admit non-circular floes.

Previous work also exists into interaction theory for multiple floating bodies, with application to ice floes. By using local coordinate systems and Graf's addition formula (see Abramowitz and Stegun, 1964, chapter 9), Peter and Meylan (2004) extended Meylan (2002) to a finite number of such bodies. However, the computational cost of calculating the interactions of a finite number of bodies that is large enough to represent situations in the MIZ is unmanageable. Instead, it is effective to study periodic problems that involve an infinite number of identical floes as a model of the MIZ. As such, Peter et al. (2006) and Wang et al. (2007) both solve for a straight line array of identical ice floes on a fluid domain that stretches to infinity in all lateral directions. The former work uses Graf's formula, as in Peter and Meylan (2004), to calculate the floe-floe interactions, and implements the periodicity to simplify the resulting system. Whereas, in the latter, a periodic Green's function provides a method of solution.

As in Peter et al. (2006) and Wang et al. (2007), we will construct a solution method for a straight-line array of equispaced, identical bodies, floating on an infinite fluid surface. Our approach to the

problem is markedly different to that of the previous authors from the outset. However, we begin by posing the problem in the alternative setting of a single channel that contains a single floe and has appropriate periodicity conditions applied on its lateral walls, which was the idea employed by Porter and Porter (2001) for free-surface flows over periodic topography. The MMA of Bennetts et al. (2007) is then used to produce a new set of governing equations that exist in the horizontal plane only and separates the free-surface and ice-covered fluid domains. A single-mode approximation was generated in an identical manner for this problem by Bennetts and Squire (2008). Thus, this paper extends that work in the same way that Bennetts et al. (2007) extends Porter and Porter (2004).

Our use of the MMA is consistent with Bennetts et al. (2009b), which allows us to easily accommodate their solution for floes that vary in thickness (axisymmetrically) and possess a non-zero draught into the model. This requires the use of a Fourier expansion to leave a set of ordinary differential equations (ODEs) that are solved numerically over the radius of the floe. The interaction theory in the free-surface domain is based on a matrix of Green's functions, which, when combined with Green's theorem, provides an integral expression for the unknown functions. These two different representations are then matched at their interface, the ice edge, to complete the solution process.

The study of infinite arrays has many other applications in hydrodynamical problems and other physical situations, for example electromagnetic scattering. There have therefore been many mathematical advances in this area that have arisen from investigations not motivated primarily by scattering by sea-ice. Recently, methods based on the solution for an infinite array have been used to produce solutions for a semi-infinite array (see Linton et al., 2007; Peter and Meylan, 2007) and approximations for long, finite arrays (see Thompson et al., 2008).

As we have already alluded to, our chosen solution method for the single-line array will provide the basis for a model of a typical situation in a polar or subpolar MIZ in a forthcoming study. This work makes use of the particularly simple structure of the expression for the scattered field from the single-line array, which is given by our method, to extend to a multiple-line array. The results found from such geometrical configurations will be used to draw inferences about the way in which waves penetrate through packs of floes into the inner mass of continuous sea-ice.

2. Boundary value problem

We wish to solve the problem of a straight-line array of identical axisymmetric floes, which are permitted to vary in thickness (through both their upper and lower surfaces) and have a non-zero draught. The Cartesian coordinates x and y will be used to denote horizontal position, with z being the vertical coordinate. The plane $z=0$ is set to coincide with the equilibrium fluid surface and the bed (considered flat and of finite depth) lies at $z=-h$. Without loss of generality, we orientate our horizontal coordinates so that the centre of the floes occupy the y-axis, with one floe having its centre at the origin $(x,y)=(0,0)$. If we now let the distance between the centre of adjacent floes be $2y_0$, for some positive constant y_0, then the centre of the floes are located at the points $y=2ny_0$ $(n\in\mathbb{Z})$.

Assuming the regular properties of linear motion, the motion of the fluid may be defined through a reduced *velocity potential*, $\hat{\Phi}=\hat{\Phi}(x,y,z)$, which, for time-harmonic conditions, is such that the velocity field is retrieved from $\Re\mathrm{e}\{(g/i\omega)(\partial_x,\partial_y,\partial_z)\cdot(\hat{\Phi}\mathrm{e}^{-\mathrm{i}\omega t})\}$. Here $g\approx 9.81\,\mathrm{m\,s^{-2}}$ denotes the acceleration due to gravity and ω is a prescribed angular frequency. When forced by a wave the underside of each floe experiences small-amplitude oscillations. The position of the fluid-ice interface is then defined to be

$$z=-d(x,y)+\Re\mathrm{e}\{W(x,y)\mathrm{e}^{-\mathrm{i}\omega t}\},$$

for (x,y) within the ice-covered regions. We use $z=-d$ to denote the equilibrium position of the

lower surface of the floes, with $d = 0$ outside of the ice-covered region. The function W is the reduced *displacement* of the floes and, for consistency, we may set W to define the free-surface outside of the ice-covered regions (although this will not be used in practice). We are now required to solve for the velocity potential, $\hat{\Phi}$, in the fluid domain and the displacement, W, within the ice-covered fluid regions.

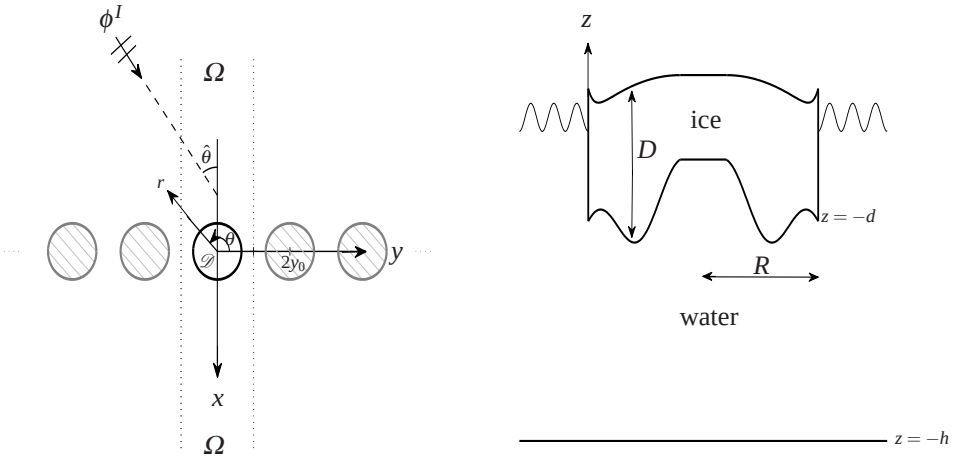

FIG. 1. Plan view of the geometrical configuration and cross-section of axisymmetric floe.

The array is forced by a plane wave, ϕ^I say, of wavenumber k_0, which, without loss of generality, we assume to propagate from the far-field $x \to -\infty$ at the oblique angle $\hat{\theta}$ ($0 \leqslant \hat{\theta} < \pi/2$) with respect to the x-axis (see figure 1). This induces a periodicity condition, namely that

$$\hat{\Phi}(x,y+2y_0,z) = \mathrm{e}^{2\mathrm{i}u_0y_0}\hat{\Phi}(x,y,z), \quad \partial_y\hat{\Phi}(x,y+2y_0,z) = \mathrm{e}^{2\mathrm{i}u_0y_0}\partial_y\hat{\Phi}(x,y,z), \tag{2.1}$$

with similar expressions holding for the displacement function W. The quantity $u_0 = k_0 \sin\hat{\theta}$ is related to the forcing wave and is considered known during the formulation of the scattering problem.

It is therefore possible to solve for the infinite array by considering a single channel of width $2y_0$ in the y-direction. For simplicity, we will take this channel to be

$$(x,y) \in \Omega = \{x, y : -\infty < x < \infty, -y_0 < y < y_0\}$$

and $z \in (-h,-d)$. At this point we define the single floe contained within this channel to occupy the region $(r,\theta) \in \mathscr{D} = \{r, \theta : r < R, 0 \leqslant \theta < 2\pi\}$, where R denotes the radius of the floe. As the floe is circular, we will find it convenient to use the polar coordinates (r,θ) in place of x and y in $\mathscr{D}$, which are such that $x = r\cos\theta$ and $y = r\sin\theta$. Under the imposed axisymmetric conditions in $\mathscr{D}$ we have $d = d(r)$, and also $D = D(r)$, where D denotes the thickness of the ice. Furthermore, we define $H(r) = h - d(r)$ to be the fluid depth beneath the floe.

Within the fluid domain the velocity potential must satisfy Laplace's equation

$$\nabla^2\hat{\Phi} + \partial_z^2\hat{\Phi} = 0 \quad ((x,y) \in \Omega, z \in (-h,-d)),$$

where $\nabla = (\partial_x, \partial_y)$ or $\nabla = (\cos(\theta)\partial_r - (1/r)\sin(\theta)\partial_\theta, \sin(\theta)\partial_r + (1/r)\cos(\theta)\partial_\theta)$, depending on the context, and on the bed ($z = -h$) the no-flow condition $\partial_z\hat{\Phi} = 0$ for $(x,y) \in \Omega$ holds. At the fluid-ice

interface ($z=-d$) we have high-order conditions that define the dynamics of the floe's oscillations and in doing so couple the velocity potential to the displacement function. These conditions are given as

$$(1-\sigma\alpha)W+\mathscr{L}W-\hat{\Phi}=0 \quad \nabla d\cdot\nabla\hat{\Phi}+\partial_z\hat{\Phi}=0 \quad ((x,y)\in\mathscr{D}, z=-d),$$

where

$$\mathscr{L}\equiv\nabla^2(\beta\nabla^2)-\frac{1}{r^2}(1-\nu)\{r(\partial_r\beta)\partial_r^2+r(\partial_r^2\beta)\partial_r+(\partial_r^2\beta)\partial_\theta^2\},$$

(see Porter and Porter, 2004). The various quantities are defined as $\nu=0.3$, which is Poisson's ratio for sea-ice, $\sigma=\omega^2/g$, the frequency parameter, $\alpha=\alpha(r)=\rho_i D/\rho_w$, the scaled mass of the floe, and $\beta=\beta(r)=ED^3/12(1+\nu)\rho_w g$, the scaled flexural rigidity of the floe. Further parameters have been introduced in these definitions and they are: the density of the ice $\rho_i=922.5$ kg m^{-3}; the density of the fluid $\rho_w=1025\,\mathrm{kg\,m^{-3}}$; and Young's modulus $E=5\times10^9$ Pa. At the edge of the floe, $\Gamma=\{x,y: x^2+y^2=R\}\equiv\{r,\theta: r=R, 0\leqslant\theta<2\pi\}$, two further dynamic conditions must hold, which state that the bending moment and shearing stress must vanish. These conditions are expressed as $\mathscr{B}W=0$ and $\mathscr{S}W=0$ respectively, where

$$\mathscr{B}\equiv\beta\nabla^2-\frac{1}{r}(1-\nu)\beta\{\partial_r+\frac{1}{r}\partial_\theta^2\}, \tag{2.2a}$$

and

$$\mathscr{S}\equiv\partial_r(\beta\nabla^2)-\frac{1}{r}(1-\nu)\{(\partial_r\beta)(\partial_r+\frac{1}{r}\partial_\theta^2)-\beta\partial_r(\frac{1}{r}\partial_\theta^2)\}, \tag{2.2b}$$

(see Bennetts et al., 2009b).

We translate the periodicity of the solution given in equations (2.1) into transition conditions on the sides of the channel to give

$$\hat{\Phi}(x,y_0,z)=\mathrm{e}^{2\mathrm{i}u_0y_0}\hat{\Phi}(x,-y_0,z), \quad \partial_y\hat{\Phi}(x,y_0,z)=\mathrm{e}^{2\mathrm{i}u_0y_0}\partial_y\hat{\Phi}(x,-y_0,z). \tag{2.3}$$

The problem is fully defined by prescribing the form of the solution in the far-field $x\to\pm\infty$. As indicated earlier, there exists a single incident wave $\phi^I(x,y)\cosh\{k_0(z+h)\}$, where $\phi^I(x,y)=\mathrm{e}^{\mathrm{i}(v_{0,0}x+u_0y)}$, which propagates from $x\to-\infty$ towards the array of floes (see figure 1). This incident wave is partially reflected and partially transmitted by the array and the following radiation conditions hold

$$\hat{\Phi}(x,y,z)\sim\Big\{\mathrm{e}^{\mathrm{i}(v_{0,0}x+u_0y)}+\sum_{s\in S}R_s\mathrm{e}^{\mathrm{i}(-v_{0,s}x+u_sy)}\Big\}\cosh\{k_0(z+h)\} \tag{2.4a}$$

as $x\to-\infty$, and

$$\hat{\Phi}(x,y,z)\sim\Big\{\sum_{s\in S}T_s\mathrm{e}^{\mathrm{i}(v_{0,s}x+u_sy)}\Big\}\cosh\{k_0(z+h)\} \tag{2.4b}$$

as $x\to\infty$. In the above $u_s=u_0+s\pi/y_0$ and $v_{0,s}=\sqrt{k_0^2-u_s^2}$ ($s\in S$), and S is the subset of natural numbers for which the $v_{0,s}$ are real. The quantity k_0 is the propagating wavenumber that will be defined shortly. These radiation conditions express the form of the solution in the far-field as a finite number of propagating waves that travel with known angles. All remaining motions generated in the scattering process have evanesced by the time they reach the far-field.

3. Multi-mode approximation

Due to the complexity presented by the variable ice-thickness and non-zero draught, the problem outlined in the previous section is deemed unsolvable by direct methods. Instead we will employ the approximation technique that was outlined in Bennetts et al. (2007). In that work a variational principle was given that is equivalent to the full-linear governing equations of a system of fluid with partial ice-covering in three-dimensions, for which the problem considered here of a periodic line array of circular floes is a subset. This variational principle allowed Bennetts et al. to define a hierarchy of increasingly accurate approximations, capable of reproducing the full-linear solution to any chosen tolerance, which they were able to calculate for two-dimensional geometries. We will extend this approach to the current problem.

Following Bennetts et al. we will retrieve the full-linear solution by implementing a type of Rayleigh-Ritz approximation that restricts the vertical motion of the velocity potential, $\hat{\Phi}$, to a finite-dimensional space of dimension $N+1$ ($N=0,\dots$), spanned by a set of *vertical modes*. Consequently, the displacement function, W, is also approximated but only indirectly through its relation to the potential.

The restriction of the vertical motion in combination with the variational principle given in Bennetts et al. has the effect of vertically averaging the problem's dependence on z. As we will see, a new set of governing equations is then generated that are independent of this coordinate.

Our approximation can be made arbitrarily close to the full-linear solution by selecting the dimension $N+1$ to be suitably large. However, we wish to balance this with a desire to minimise the computational cost needed to gain solutions and we therefore seek to encapsulate the key features of the vertical motion in a relatively small number of modes. As such we employ the following multiple-mode expansions of the vertical dependence of the potential

$$\hat{\Phi}(x,y,z) \approx \begin{cases} \phi(x,y) = \sum_{n=0}^{N} \phi_n(x,y)\zeta_n(z) & ((x,y) \in \Omega/\mathscr{D}), \\ \psi(r,\theta) = \sum_{n=0}^{N} \psi_n(r,\theta)\chi_n(r,z) & ((x,y) \in \mathscr{D}), \end{cases} \tag{3.1}$$

where the vertical modes are defined as $\zeta_n(z) = \cosh\{k_n(z+h)\}$ and $\chi_n(r,z) = \cosh\{\kappa_n(r)(z+h)\}$. It has been shown in various other problems involving partial ice-covering (Bennetts, 2007; Bennetts et al., 2007) that the above choice of expansion, in which we partition the approximation between the ice-covered and ice-free regions, is capable of providing accurate results for relatively small dimensions. In the free-surface fluid region the vertical modes, ζ_n, are defined by the quantities k_n, which are the roots k of the free-surface dispersion relation

$$k\tanh(kh) = \sigma, \tag{3.2}$$

such that k_0 is real and positive and the k_n ($n=1,\dots$) lie on the positive imaginary axis and are ordered in increasing magnitude, that is $-\mathrm{i}k_n < -\mathrm{i}k_{n+1}$. The quantities κ_n, that define the vertical modes in the region of ice-covered fluid, are the roots κ of the ice-covered dispersion relation

$$(1-\sigma\alpha+\beta\kappa^4)\kappa\tanh(\kappa H) = \sigma, \tag{3.3}$$

and are functions of the radial coordinate due to the axisymmetrically varying mass $\alpha = \alpha(r)$, flexural rigidity $\beta = \beta(r)$ and fluid depth $H = H(r)$. Similarly to the roots of the free-surface dispersion relation, we set the primary root, κ_0, to be positive and real, and κ_n ($n=1,\dots$) to be roots of increasing

magnitude that lie on the positive imaginary axis. The complex roots of equation (3.3), which under some circumstances may bifurcate to become purely imaginary, are omitted from the approximation as the vertical modes that they define are linearly dependent on those we have included (for details see Bennetts et al., 2007). We note that the expansions (3.1) produce the vertical modes that are found when separation solutions are sought in the respective ice-free and ice-covered regions.

When our approximate form of the potential (3.1) is applied to the variational principle given in Bennetts et al. (2007) a new set of governing equations is created. From these new equations we must calculate the unknown functions ϕ_n and ψ_n $(n = 0,\ldots,N)$, along with the corresponding approximation of the displacement function $w(r,\theta) \approx W(x,y)$. The approximation that is generated through this combination of expansion and variational principle we will term the *multi-mode approximation* (MMA).

In the free-surface region it remains to solve the Helmholz equations

$$\nabla^2 \boldsymbol{\Phi} + K_0^2 \boldsymbol{\Phi} = \mathbf{0} \quad ((x,y) \in \Omega/\mathscr{D}), \tag{3.4}$$

where the vector of solutions is

$$\boldsymbol{\Phi} = \boldsymbol{\Phi}(x,y) = (\phi_0(x,y),\ldots,\phi_N(x,y))^T,$$

and the matrix $K_0 = \mathrm{diag}\{k_0,\ldots,k_N\}$. For the disc $\mathscr{D}$ in which the fluid is ice-covered, we now have the system of second-order equations

$$\frac{1}{r}\partial_r(rA\partial_r\boldsymbol{\Psi}) + \widetilde{D}\partial_r\boldsymbol{\Psi} + \left(B + \frac{1}{r^2}A\partial_\theta^2\right)\boldsymbol{\Psi} + \sigma C\mathbf{f}w = \mathbf{0} \quad ((r,\theta) \in \mathscr{D}), \tag{3.5a}$$

which is coupled to the fourth-order equation

$$(1-\sigma\alpha)w + \mathscr{L}w - \mathbf{f}^T C\boldsymbol{\Psi} = 0 \quad ((r,\theta) \in \mathscr{D}). \tag{3.5b}$$

In the above the vector of unknowns is

$$\boldsymbol{\Psi} = \boldsymbol{\Psi}(r,\theta) = (\psi_0(r,\theta),\ldots,\psi_N(r,\theta))^T,$$

and we define the $(N+1)$-length vector $\mathbf{f} = (1,\ldots,1)^T$ and $(N+1)$-square size matrix $C = C(r) = \mathrm{diag}\{\chi_0(r,-h),\ldots,\chi_N(r,-h)\}$. The matrices of coefficients $A = A(r)$, $B = B(r)$, and $\widetilde{D} = \widetilde{D}(r)$ have entries that contain the averaged values of the vertical dependence, which are calculated from integrals of the modes χ_n and their derivatives. These are

$$\{A\}_{j+1,i+1} = \int_{-h}^{-d} \chi_j\chi_i \,\mathrm{d}z,, \quad \{\widetilde{D}\}_{j+1,i+1} = \int_{-h}^{-d} \{\chi_j(\partial_r\chi_i) - \chi_i(\partial_r\chi_j)\} \,\mathrm{d}z, \tag{3.6a}$$

and

$$\{B\}_{j+1,i+1} = \int_{-h}^{-d} \chi_j(\partial_z^2\chi_i) \,\mathrm{d}z - [\chi_j(\partial_z\chi_i)]_{z=-h}^{-d} + \partial_r\int_{-h}^{-d} \chi_j(\partial_r\chi_i) \,\mathrm{d}z - \int_{-h}^{-d} (\partial_r\chi_j)(\partial_r\chi_i) \,\mathrm{d}z \tag{3.6b}$$

for $i, j = 0,\ldots,N$. The explicit calculation of the quantities (3.6a–b) follows that described by Bennetts et al. (2007).

In (3.1) there is a partitioning of the solution between the ice-covered and free-surface regions, which has the effect of creating a discontinuity in the velocity potential at the edge of the floe $(r,\theta \in \Gamma)$.

Jump conditions are provided by the variational principle at the discontinuity and were calculated for a circular floe by Bennetts et al. (2009b) as

$$P_+^T\Psi = P_-^T\Phi, \quad P_+^{-1}\{A\partial_r\Psi + Q\Phi\} = P_-^{-1}A_-\partial_r\Phi \quad ((r,\theta)\in\Gamma), \tag{3.7}$$

where $P_+ = A$,

$$\{P_-\}_{j+1,i+1} = \int_{-h}^{-d}\zeta_j\chi_i\,\mathrm{d}z, \quad \{A_-\}_{j+1,i+1} = \int_{-h}^{-d}\zeta_j\zeta_i\,\mathrm{d}z, \quad \{Q\}_{j+1,i+1} = \int_{-h}^{-d}\chi_j\partial_r\chi_i\,\mathrm{d}z$$

for $i,j = 0,\ldots,N$, and we have made use of the flat bed depth away from the floe.

Although the discontinuity in the velocity potential is an unphysical feature of our approximation, the continuity of fluid pressure and velocity will be regained as the number of vertical modes is increased and convergence to the full-linear solution is achieved. Rather than having a detrimental effect on the MMA, our choice to partition the solution in equation (3.1) in fact allows for high accuracy with a relatively low number of modes as we are able to use the natural modes for each respective region. As the displacement is indirectly approximated, the remaining conditions applied at the ice edge are still $\mathscr{B}w = \mathscr{S}w = 0$ $(r,\theta\in\Gamma)$.

The transition boundary conditions for $\widehat{\Phi}$, given in equations (2.3), are similarly satisfied by ϕ, so that

$$\phi_n(x,y_0) = \mathrm{e}^{2\mathrm{i}u_0y_0}\phi_n(x,-y_0), \quad \partial_y\phi_n(x,y_0) = \mathrm{e}^{2\mathrm{i}u_0y_0}\partial_y\phi_n(x,-y_0), \tag{3.8}$$

for $n = 0,\ldots,N$. Similarly, the radiation conditions (2.4) are easily retained in the approximation

$$\phi_0(x,y) \sim \begin{cases} \mathrm{e}^{\mathrm{i}(v_{0,0}x+u_0y)} + \displaystyle\sum_{s\in S} R_s\mathrm{e}^{\mathrm{i}(-v_{0,s}x+u_sy)} & (x\to-\infty), \\ \displaystyle\sum_{s\in S} T_s\mathrm{e}^{\mathrm{i}(v_{0,s}x+u_sy)} & (x\to\infty), \end{cases} \tag{3.9}$$

and $\phi_n\sim 0$ as $x\to\pm\infty$ $(n=1,\ldots,N)$. Notice that this is a consequence of our choice of the vertical mode ζ_0 in the free-surface region and is an important feature of the approximation.

4. Solution Process

As it now stands, we may decompose our task into two disjoint problems. In the first, we consider the solution ϕ of the free-surface problem posed by the system of Helmholz equations (3.4) in $\Omega/\mathscr{D}$, subject to the transition conditions (3.8a–b) and radiation conditions (3.9). Scattering is caused by the relation to the, as yet, unknown function ψ and its radial derivative on the boundary Γ. For the second problem we must obtain ψ and w as the solutions to the system of differential equations (3.5a–b) in the disc $\mathscr{D}$, where w satisfies the bending moment and shearing stress conditions at the edge Γ. Forcing is provided through ψ from the jump conditions (3.7) at Γ. Once the solutions have been obtained in their respective regions, up to unknown factors, we will complete the solution through the imposition of these jump conditions. As the two domains Ω and $\mathscr{D}$ are fundamentally different, one being structured on Cartesian coordinates, the other on polar coordinates, we are unable obtain a solution through use of any direct modal expansion. Instead, we will pursue a method in which we treat each domain independently, and finally match the derived representations at their common boundary (Γ).

4.1 *The free-surface domain*

Consider first the free-surface domain $\Omega/\mathscr{D}$. Let the $(N+1)$-square matrix of Green's function $G = G(x,y|\xi,\eta)$ be defined over the entire channel Ω in the absence of the floe, so that it satisfies the equations

$$\nabla^2 G + K^2 G = \delta(x-\xi)\delta(y-\eta)I \quad ((x,y)\in\Omega),$$

where I denotes the identity matrix of dimension $N+1$. On the lateral boundaries $y = \pm y_0$, we impose the transition conditions

$$G(x,y_0|\xi,\eta) = \mathrm{e}^{-2\mathrm{i}u_0 y_0} G(x,-y_0|\xi,\eta), \quad \partial_y G(x,y_0|\xi,\eta) = \mathrm{e}^{-2\mathrm{i}u_0 y_0}\partial_y G(x,-y_0|\xi,\eta),$$

which, we note, are the exact opposite of those satisfied by ϕ. Finally, we require that G represents outgoing waves in the far-fields $x \to \pm\infty$.

Using an expansion in the modes $\mathrm{e}^{-\mathrm{i}u_m Y}$ $(m\in\mathbb{Z})$, with $Y = y-\eta$, the matrix of Green's functions G, defined above, is easily found to be

$$G(x,y|\xi,\eta) = \frac{1}{4\mathrm{i}y_0}\sum_{m=-\infty}^{\infty} V_m^{-1}\mathrm{e}^{\mathrm{i}V_m|X|}\mathrm{e}^{-\mathrm{i}u_m Y}, \tag{4.1}$$

where $X = x-\xi$. The matrices $V_m = \mathrm{diag}\{v_{0,m},\ldots,v_{N,m}\}$ and $\mathrm{e}^{\mathrm{i}V_m x} = \mathrm{diag}\{\mathrm{e}^{\mathrm{i}v_{0,m}x},\ldots,\mathrm{e}^{\mathrm{i}v_{N,m}x}\}$ for the scalar values $v_{n,m} = \sqrt{k_n^2 - u_m^2}$, which extends the earlier definition of $v_{0,s}$. The single-mode ($N=0$) version of G has been calculated and utilised previously for periodic three-dimensional geometries with free-surface flows (see Porter and Porter, 2001) and to form an approximation for the current problem (see Bennetts and Squire, 2008).

In the representation (4.1) we have implicitly assumed that the frequency and angle of the incident wave do not combine with the spacing of the floes to produce $v_{0,m} = 0$ for some $m\in\mathbb{Z}$. In such resonant cases one or more waves travel parallel to the array itself and special attention must be made to construct a solution method. Using Graf's addition formula for a similar periodic array, Linton and Thompson (2007) recently showed that by considering certain quantities as functions of the incident angle and seeking Taylor expansions they could circumvent the singularities that usually prevent a solution under resonant conditions. An analogous approach could be adopted in our method to provide solutions for the cases in which there exists an $m\in\mathbb{Z}$ such that $v_{0,m} = 0$, although we do not pursue the idea in our current study and these isolated situations are disregard for the remainder of this work.

We will make use of Green's second identity in the form

$$\iint_{\Omega_0}\{u(\nabla^2 v) - v(\nabla^2 u)\}\,\mathrm{d}x\,\mathrm{d}y = \int_{\delta\Omega_0}\{u(\partial_n v) - v(\partial_n u)\}\,\mathrm{d}s, \tag{4.2}$$

where u and v are suitably differentiable scalar functions defined over the domain Ω_0 with the simple boundary $\delta\Omega_0$. Applying equation (4.2) to the vector Φ and matrix G over the domain $\Omega/\mathscr{D}$, in which we have made the natural extensions of the result to arrays, we deduce the representations

$$\Phi(\xi,\eta) = \Phi^I(\xi,\eta) - R\int_0^{2\pi}\Big\{(\partial_r G)\Phi - G(\partial_r\Phi)\Big\}_{r=R}\mathrm{d}\theta, \tag{4.3a}$$

for $(\xi,\eta)\in\Omega/\mathscr{D}$, and

$$\frac{1}{2}\Phi(\xi,\eta) = \Phi^I(\xi,\eta) - R\int_0^{2\pi}\Big\{(\partial_r G)\Phi - G(\partial_r\Phi)\Big\}_{r=R}\mathrm{d}\theta, \tag{4.3b}$$

for $(\xi,\eta)\in\Gamma$. The vector equivalent of Φ for the incident wave is Φ^I, that is

$$\Phi^I(x,y)=(\mathrm{e}^{\mathrm{i}(v_{0,0}x+u_0y)},0,\ldots,0)^T.$$

The latter of these representations provides us with the necessary boundary data with which we may connect ϕ with ψ at their common boundary, whereas the first will give us a means of calculating the velocity potential across the free-surface region once its value and the value of its radial derivative have been obtained on the ice edge.

For $|\xi|\geqslant R$ the matrix of Green's functions G is smooth on the contour $(x,y)\in\Gamma$. Due to the resulting simplifications in the integral appearing in expression (4.3a), it is possible to write Φ in a more appealing fashion, which is

$$\Phi(\xi,\eta)=\begin{cases}\Phi^I(\xi,\eta)+\displaystyle\sum_{m=-\infty}^{\infty}\mathrm{e}^{-\mathrm{i}V_m\xi}\mathbf{R}_m\mathrm{e}^{\mathrm{i}u_m\eta} & (\xi\leqslant R),\\ \displaystyle\sum_{m=-\infty}^{\infty}\mathrm{e}^{\mathrm{i}V_m\xi}\mathbf{T}_m\mathrm{e}^{\mathrm{i}u_m\eta} & (\xi\geqslant R).\end{cases}\tag{4.4}$$

The vectors $\mathbf{R}_m$ and $\mathbf{T}_m$ contain the reflected and transmitted amplitudes respectively and are calculated from

$$\mathbf{R}_m=\frac{R}{4\mathrm{i}y_0}V_m^{-1}\int_0^{2\pi}\left[\mathrm{e}^{\mathrm{i}V_mx}\{(\partial_r\Phi)-\mathrm{i}(\cos\theta V_m-\sin\theta u_mI)\Phi\}\mathrm{e}^{-\mathrm{i}u_my}\right]_{r=R}\mathrm{d}\theta,\tag{4.5a}$$

and

$$\mathbf{T}_m=\delta_{0,m}\mathbf{I}_1+\frac{R}{4\mathrm{i}y_0}V_m^{-1}\int_0^{2\pi}\left[\mathrm{e}^{-\mathrm{i}V_mx}\{(\partial_r\Phi)+\mathrm{i}(\cos\theta V_m+\sin\theta u_mI)\Phi\}\mathrm{e}^{-\mathrm{i}u_my}\right]_{r=R}\mathrm{d}\theta,\tag{4.5b}$$

once Φ and $\partial_r\Phi$ are known on Γ. Here $\delta_{i,j}=0$ $(i\neq j)$ and $\delta_{i,i}=1$, and $\mathbf{I}_1$ represents the first column of the identity matrix I. Calculation of the integrals in equations (4.5a–b) will be explained in further detail at a later point, as by that stage we will have a simpler expression for the unknown functions at the ice edge.

To find Φ when $|\xi|<R$ is a more difficult task as we encounter the discontinuities that exist in the Green's functions at the point $x=\xi$ that require the integrals in equation (4.3a) to be divided into their respective intervals. For this reason we are unable to separate the field variables from the integrals in any logical way akin to that which produced expression (4.4). We must also be wary of the singularity present in the Green's functions when $(x,y)=(\xi,\eta)$, which will lead to slow convergence when the field variables are in a vicinity of the contour Γ. However, in §4.3, as part of our solution procedure, we will outline a method for writing the Green's functions using a Kummer transformation, which allows for cost-effective integration and may also be applied for the purpose of evaluating the free-surface velocity potential in this situation.

At this point we emphasise that the method described in this section is applicable to an array in which the ice floes are of a more general shape than the circular one considered here, and solutions for floes that will conform to our approach are currently under construction. However, we note that the circular shape of the boundary Γ strongly influences the way in which we treat the integrals in equation (4.3b) and an extension to non-circular floes would require a suitable modification of the solution procedure.

4.2 *The ice-covered domain*

Next, we consider the ice-covered domain $\mathscr{D}$. The method we will utilise is a modification of that of Bennetts et al. (2009b), who considered a solitary axisymmetric ice floe.

Let the unknowns be written in terms of the Fourier expansions

$$\Psi(r,\theta) \approx \sum_{m=-M}^{M} \Psi_m(r)\mathrm{e}^{\mathrm{i}m\theta}, \quad w(r,\theta) \approx \sum_{m=-M}^{M} w_m(r)\mathrm{e}^{\mathrm{i}m\theta}, \tag{4.6}$$

which, for the purposes of numerical calculation, we have truncated to a finite dimension that will provide sufficient accuracy. Due to the assumed axisymmetry of the geometry, the governing equations (3.5a–b) decouple into a set of ODEs in the radial coordinate that may be solved independently for each Fourier mode. As in Bennetts et al., we choose to write these decoupled equations as the (N+3)-system of second-order equations

$$\frac{1}{r}\partial_r(r\mathscr{A}\partial_r\mathbf{U}_m) + \widetilde{\mathscr{D}}\partial_r\mathbf{U}_m + \mathscr{B}^{(m)}\mathbf{U}_m = \mathbf{0} \quad (m=-M,\ldots,M), \tag{4.7}$$

for $0<r<R$, in which a prime denotes differentiation with respect to r. These equations are to be solved for the vectors $\mathbf{U}_m = (\Psi_m, w_m^{(1)}, w_m^{(2)})^T$, where $w_m^{(1)} \equiv w_m$ and $w_m^{(2)} \equiv \beta\nabla^2 w_m$. The components of the matrices appearing in equation (4.7) are defined by

$$\{\mathscr{A}\}_{j,i} = \{A\}_{j,i}, \quad \{\mathscr{B}^{(m)}\}_{j,i} = \{B\}_{j,i} - \frac{m^2}{r^2}\{A\}_{j,i}, \quad \{\widetilde{\mathscr{D}}\}_{j,i} = \{\widetilde{D}\}_{j,i} \quad (i,j=1,\ldots,N+1),$$

$$\{\mathscr{A}\}_{N+2,N+2} = \{\mathscr{A}\}_{N+3,N+3} = 1, \quad \{\mathscr{B}^{(m)}\}_{i,N+2} = \sigma\mathbf{I}_i^T C\mathbf{f} \quad (i=1,\ldots,N+1),$$

$$\{\mathscr{A}\}_{N+3,N+2} = -(1-\nu)\frac{1}{r}(\partial_r\beta), \quad \{\mathscr{B}^{(m)}\}_{N+2,N+3} = -\beta^{-1}, \quad \{\mathscr{B}^{(m)}\}_{N+3,j} = -\mathbf{f}^T C\,\mathbf{I}_j$$

for $j=1,\ldots,N+1$, and

$$\{\mathscr{B}\}^{(m)}_{N+2,N+2} = \{\mathscr{B}\}^{(m)}_{N+3,N+3} = -\frac{m^2}{r^2}, \quad \{\mathscr{B}^{(m)}\}_{N+3,N+2} = (1-\nu)(\partial_r^2\beta)\frac{m^2}{r^2} + 1 - \sigma\alpha,$$

with all unspecified values equal to zero. We have used $\mathbf{I}_j$ $(j=1,\ldots,N+1)$ to denote the vector of length $N+1$ with the only non-zero entry being a 1 in the jth position. The matrices A, B and $\tilde{D}$ were previously defined in equations (3.6a–c).

At the centre of the floe we require that the solution is bounded. However, the use of the polar coordinates introduces a singularity at this point. In order to deal with this efficiently in our numerical solution, we mimic Bennetts et al. by assuming the existence of a disc of arbitrarily small radius ε around the centre of the floe, within which the geometry of the ice is uniform. These authors then showed that in this region the vectors $\mathbf{U}_m$ can be calculated explicitly as

$$\mathbf{U}_m(r) = \mathscr{C}\,\mathscr{J}_m(r)\mathbf{A}_m \quad (m=-M,\ldots,M), \tag{4.8}$$

where $\mathscr{J}_m(r) = \mathrm{diag}\{\mathrm{J}_m(\kappa_0 r),\ldots,\mathrm{J}_m(\kappa_N r),\mathrm{J}_m(\mu_1 r),\mathrm{J}_m(\mu_2 r)\}$ is a diagonal matrix containing Bessel functions of the first kind of order m, J_m, and where $\mathbf{A}_m$ is a currently unknown $(N+3)$-length vector of constants. The matrix $\mathscr{C}$ is defined by

$$\{\mathscr{C}\}_{n,n} = 1, \quad \{\mathscr{C}\}_{N+2,n} = \sigma^{-1}\kappa_{n-1}\sinh(\kappa_{n-1}H),$$

and

$$\{\mathscr{C}\}_{n,N+i} = \{\mathbf{g}(\mu_{i-1})\}_n, \quad \{\mathscr{C}\}_{N+2,N+i} = 1, \quad \{\mathscr{C}\}_{N+3,N+i} = -\beta\mu_{i-1}^2,$$

for $n = 1,\ldots,N+1$ and $i = 2,3$. Here, the vector $\mathbf{g} = \mathbf{g}(\mu)$ is defined by

$$A\mathbf{g} + \beta(K^2 + \mu^2 I)KS\mathbf{f} = \mathbf{0},$$

where $K = \text{diag}\{\kappa_0,\ldots,\kappa_N\}$ and $S = \{\sinh(\kappa_0 H),\ldots,\sinh(\kappa_N H)\}$, and the values μ_i $(i = 1,2)$ are the roots of

$$(\beta\mu^4 + 1 - \sigma\alpha) + \beta\mathbf{f}^T CA^{-1}(K^2 + \mu^2 I)KS\mathbf{f} = 0,$$

that exist in the upper-half complex plane.

By using expression (4.8) for $r < \varepsilon$ we have eliminated the singularity introduced by the radial coordinates analytically. In practice the requirement of an inner disc of uniform geometry does not compromise the generality of the geometry, as we simply select our desired ice thickness and let the value of ε tend to zero until we achieve convergence in our results.

We are now required to join our analytic expressions for the solution within the disc of uniform geometry to the annulus of varying geometry. Bennetts et al. (2009b) showed these conditions to be

$$[\Psi_m]_{\varepsilon_-}^{\varepsilon_+} = [A\partial_r\Psi_m + Q\Psi_m]_{\varepsilon_-}^{\varepsilon_+} = \mathbf{0}, \tag{4.9a}$$

and

$$\left[w_m^{(1)}\right]_{\varepsilon_-}^{\varepsilon_+} = \left[w_m^{(2)}\right]_{\varepsilon_-}^{\varepsilon_+} = \left[\mathscr{B}_m(w_m^{(1)}, w_m^{(2)})\right]_{\varepsilon_-}^{\varepsilon_+} = \left[\mathscr{S}_m(w_m^{(1)}, w_m^{(2)})\right]_{\varepsilon_-}^{\varepsilon_+} = 0 \tag{4.9b}$$

for $m = -M,\ldots,M$, where

$$\mathscr{B}_m(w_m^{(1)}, w_m^{(2)}) \equiv w_m^{(2)} - (1-\nu)\beta\left(\frac{1}{r}\partial_r - \frac{m^2}{r^2}\right)w_m^{(1)}, \tag{4.10a}$$

and

$$\mathscr{S}_m(w_m^{(1)}, w_m^{(2)}) \equiv \partial_r w_m^{(2)} - (1-\nu)\left\{(\partial_r\beta)\left(\frac{1}{r}\partial_r - \frac{m^2}{r^2}\right)w_m^{(1)} + \frac{m^2}{r}\beta\partial_r\left(\frac{1}{r}w_m^{(1)}\right)\right\}. \tag{4.10b}$$

Conditions (4.9a) represent approximate versions of the continuity of fluid pressure and velocity, whereas equation (4.9b) ensures the continuity of position and velocity of displacement, and the continuity of its bending moment and shearing stress.

To derive boundary data at $r = \varepsilon$ for the solutions $\mathbf{U}_m$ that satisfy equations (4.7) in the interval of varying geometry $\varepsilon < r < R$ we insert expression (4.8) into the continuity conditions (4.9a–b). These are of most use to us if we manipulate them into the form

$$\mathscr{J}_m(\mathscr{A}\mathscr{C})^{-1}\mathscr{A}\partial_r\mathbf{U}_m + \left\{\mathscr{J}_m(\mathscr{A}\mathscr{C})^{-1}\mathscr{Q}^{(m)} - (\partial_r\mathscr{J}_m)\mathscr{C}\right\}\mathbf{U}_m = \mathbf{0} \quad (r = \varepsilon), \tag{4.11}$$

for $m = -M,\ldots,M$, where the matrix $\mathscr{Q}^{(m)}$ is defined by

$$\{\mathscr{Q}^{(m)}\}_{j,i} = Q_{j,i},\ (i,j = 1,\ldots,N+1), \quad \{\mathscr{Q}^{(m)}\}_{N+i,N+i} = 1,\ (i = 2,3),$$

and $\{\mathscr{Q}^{(m)}\}_{N+3,N+2} = (1-\nu)(\partial_r\beta)(m/r)^2$, and is evaluated at $r = \varepsilon_+$. The advantage of reformulating our boundary data to be (4.11) is that the unknown amplitudes $\mathbf{A}_m$ are not present. Once the solutions $\mathbf{U}_m$ have been found these amplitudes are recovered from $\mathscr{C}\mathscr{J}_m\mathbf{A} = \mathbf{U}_m$ $(r = \varepsilon)$.

Boundary data must also be obtained for $r = R$. To do this we use the joining conditions (3.7) and the vanishing of the bending moment and shearing stress. It is a simple matter to show that the two dynamical conditions decouple to give

$$\mathscr{S}_m(w_m^{(1)}, w_m^{(2)}) = \mathscr{B}_m(w_m^{(1)}, w_m^{(2)}) = 0 \quad (m = -M, \ldots, M)$$

at $r = R$, where $\mathscr{S}_m$ and $\mathscr{B}_m$ are defined in equations (4.10a–b). In order to decouple the joining conditions we need to make an equivalent Fourier expansion of the velocity potential Φ at the ice edge, and we write

$$\Phi(R\cos\theta, R\sin\theta) \approx \sum_{m=-M}^{M} \Phi_m \mathrm{e}^{\mathrm{i}m\theta}, \quad \partial_r\Phi(R\cos\theta, R\sin\theta) \approx \sum_{m=-M}^{M} \Phi'_m \mathrm{e}^{\mathrm{i}m\theta}.$$

The modes now separate straightforwardly, and we have the conditions

$$P_+^T \Psi_m = P_-^T \Phi_m, \quad P_+^{-1}\left\{A\Psi'_m + Q\Psi_m\right\} = P_-^{-1} A_- \Phi'_m \quad (r = R), \tag{4.12}$$

for $m = -M, \ldots, M$.

At this juncture it is only possible to solve for the solutions within the ice-covered domain up to a set of unknown constants involving the velocity potential in the free-surface domain and its radial derivative, both evaluated at the ice edge, and we choose to write

$$\mathbf{U}_m(r) = [\mathbf{U}_{m,0}(r), \ldots, \mathbf{U}_{m,N}(r)]\Phi'_m(R) \quad (\varepsilon < r < R), \tag{4.13}$$

for $m = -M, \ldots, M$. The vectors $\mathbf{U}_{m,n} \equiv [\Psi_{m,n}^T, w_{m,n}^{(1)}, w_{m,n}^{(2)}]^T$ $(m = -M, \ldots, M,\, n = 0, \ldots, N)$ are numerically calculated solutions of the appropriate differential system (4.7) with boundary conditions (4.11) at $r = \varepsilon$ and

$$P_+^{-1}\left\{A\Psi'_{m,n} + Q\Psi_{m,n}\right\} = P_-^{-1} A_- \mathbf{I}_{n+1}, \quad \mathscr{S}_m(w_{m,n}^{(1)}, w_{m,n}^{(2)}) = \mathscr{B}_m(w_{m,n}^{(1)}, w_{m,n}^{(2)}) = 0 \quad (r = R).$$

The values of $\Phi'_m(R)$ will be recovered in the following section when we bring together the solutions in the ice-covered and ice-free fluid domains. Finally we note the symmetries $\mathbf{U}_m = \mathbf{U}_{-m}$ $(m = 1, \ldots, M)$, which means that only the vectors $\mathbf{U}_m$ for $m = 0, \ldots, M$ need to be found.

4.3 *Matching at the ice edge*

We now have at our disposal the expression (4.13) for each Fourier mode of the unknown functions within the ice-covered domain, $\mathbf{U}_m$ $(m = -M, \ldots, M)$, containing the as yet unknown quantities $\Phi'_m(R)$ that are the amplitudes of the equivalent Fourier mode of the radial derivative of Φ at the ice edge. Similarly, in the free-surface region we have the integral forms (4.3a–b) for the vector Φ that depend on its value and the value of its radial derivative at the ice edge. In order to complete the solution throughout the channel Ω it is therefore necessary to calculate Φ and $\partial_r\Phi$ ar $r = R$, and this is achieved by seeking their Fourier expansions and by matching the representations of the velocity potentials at their common boundary Γ.

In the previous section we found that the axisymmetric geometry of the ice floes caused the Fourier modes of the unknown functions to decouple in that region. However, the array breaks the axisymmetry of the geometry and, during the matching process, these Fourier modes will become coupled. Therefore, it is pertinent to begin by amalgamating our representations for the Fourier modes of the velocity

potential Ψ given in equation (4.13), into the single expression

$$\begin{pmatrix} \Psi_{-M}(r) \\ \vdots \\ \Psi_{M}(r) \end{pmatrix} = \widetilde{M}(r)\mathbf{f}_1,$$

where the matrix $\widetilde{M}(r)$ equals

$$\begin{pmatrix} \Psi_{-M,0}(r) & \cdots & \Psi_{-M,N}(r) & \mathbf{0} & \cdots & & & & \mathbf{0} \\ \mathbf{0} & \cdots & \mathbf{0} & \Psi_{-M+1,0}(r) & \cdots & \Psi_{-M+1,N}(r) & \mathbf{0} & \cdots & \mathbf{0} \\ \vdots & & & & & & \ddots & & \vdots \\ \mathbf{0} & \cdots & & & & & \mathbf{0} & \Psi_{M,0}(r) & \cdots & \Psi_{M,N}(r) \end{pmatrix},$$

which is of size $(2M+1)(N+1)$-square, and the vector $\mathbf{f}_1 = ((\Phi'_{-M})^T,\ldots,(\Phi'_M)^T)^T$. Letting $r \to R$ in the above equation and using the first of the jump conditions (4.12) to eliminate the vectors Ψ_m $(m=-M,\ldots,M)$, gives

$$\mathbf{f}_0 = \mathscr{M}\mathbf{f}_1, \tag{4.14}$$

where $\mathbf{f}_0 = ((\Phi_{-M})^T,\ldots,(\Phi_M)^T)^T$. The matrix $\mathscr{M}$ is calculated as $\mathscr{M} = P\widetilde{M}(R)$ where

$$P = \mathrm{diag}\{P_-^{-T}P_+^T,\ldots,P_-^{-T}P_+^T\},$$

is a block diagonal matrix of size $(2M+1)(N+1)$-square. Thus, we have a $(2M+1)(N+1)$-system of equations in (4.14) that relates the $(2M+1)(N+1)$ unknown Fourier modes of the velocity potential in the free-surface region, Φ_m, evaluated beneath the ice edge, to the $(2M+1)(N+1)$ unknown Fourier modes of its radial derivative, Φ'_m.

The remaining $(2M+1)(N+1)$ equations required to solve for the $\mathbf{f}_i$ $(i=0,1)$ are provided by our integral representation of Φ on the ice edge given in equation (4.3b). If we use our Fourier expansions of Φ and $\partial_r\Phi$ and take the $2N+1$ inner-products with respect to $\mathrm{e}^{-\mathrm{i}m\tau}$ $(m=-M,\ldots,M)$ over $\tau\in(0,2\pi)$, we may then interpret equation (4.3b) as the $(2M+1)(N+1)$-matrix system

$$\frac{1}{2}\mathbf{f}_0 = \mathbf{f}_I - R\Big(\widetilde{\mathscr{G}}\mathbf{f}_0 - \mathscr{G}\mathbf{f}_1\Big). \tag{4.15}$$

In equation (4.15) the vector $\mathbf{f}_I$ contains the inner-products of the incident wave, which are

$$\mathbf{f}_I = \frac{1}{2\pi}\begin{pmatrix} \displaystyle\int_0^{2\pi}[\Phi^I\mathrm{e}^{\mathrm{i}M\tau}]_{r=R}\,\mathrm{d}\tau \\ \vdots \\ \displaystyle\int_0^{2\pi}[\Phi^I\mathrm{e}^{-\mathrm{i}M\tau}]_{r=R}\,\mathrm{d}\tau \end{pmatrix}.$$

It is possible to rewrite the incident wave in terms of the polar coordinates (see Abramowitz and Stegun, 1964, chapter 9) and we may therefore calculate the non-trivial integrals appearing in $\mathbf{f}_I$ explicitly to be

$$\frac{1}{2\pi}\int_0^{2\pi}[\mathrm{e}^{\mathrm{i}(\nu_{0,0}x+u_0y)}\mathrm{e}^{-\mathrm{i}m\tau}]_{r=R}\mathrm{d}\tau = \mathrm{e}^{\mathrm{i}m\vartheta_{0,0}}\mathrm{J}_m(k_0R) \quad (m=-M,\ldots,M),$$

where ϑ is the angle such that $\tan\vartheta_{0,0} = \nu_{0,0}/u_0$ existing in the interval $0 < \vartheta_0 \leqslant \pi/2$. Similarly, we may now also simplify our expressions for the reflection and transmission coefficients given in equations (4.5a–b) to give

$$\mathbf{R}_p = \frac{\pi R}{2\mathrm{i}y_0} V_p^{-1} \sum_{m=-M}^{M} \mathrm{e}^{\mathrm{i}m\Theta_p} \{J_m(KR)\boldsymbol{\Phi}_m' - K(\partial_{Kr}J_m(KR))\boldsymbol{\Phi}_m\}, \tag{4.16a}$$

and

$$\mathbf{T}_p = \delta_{0,p}\mathbf{I}_1 + \frac{\pi R}{2\mathrm{i}y_0} V_p^{-1} \sum_{m=-M}^{M} \mathrm{e}^{-\mathrm{i}m\Theta_p} \{J_m(KR)\boldsymbol{\Phi}_m' - K(\partial_{Kr}J_m(KR))\boldsymbol{\Phi}_m\}, \tag{4.16b}$$

where $K = \mathrm{diag}\{k_0, \ldots, k_n\}$ and $J_m(Kr) = \mathrm{diag}\{\mathrm{J}_m(k_0 r), \ldots, \mathrm{J}_m(k_N r)\}$. The matrix $\mathrm{e}^{\mathrm{i}m\Theta_p} = \mathrm{diag}\{\mathrm{e}^{\mathrm{i}m\vartheta_{0,p}}, \ldots, \mathrm{e}^{\mathrm{i}m\vartheta_{N,p}}\}$, in which the values $\vartheta_{n,m}$ extend $\vartheta_{0,0}$ and are defined as $\tan\vartheta_{n,m} = \nu_{n,m}/u_m$, where $0 < \vartheta_{n,m} < \pi$ for $m \in S$ and $\vartheta_{n,m} \in \mathrm{i}\mathbb{R}$ for $m \notin S$.

The matrix $\mathscr{G}$ in equation (4.15) is

$$\mathscr{G} = \frac{1}{2\pi} \begin{pmatrix} \displaystyle\int_0^{2\pi}\!\!\int_0^{2\pi} [G\mathrm{e}^{\mathrm{i}(-M\theta+M\tau)}]_{r=\rho=R}\,\mathrm{d}\theta\,\mathrm{d}\tau & \cdots & \displaystyle\int_0^{2\pi}\!\!\int_0^{2\pi} [G\mathrm{e}^{\mathrm{i}(M\theta+M\tau)}]_{r=\rho=R}\,\mathrm{d}\theta\,\mathrm{d}\tau \\ \vdots & \ddots & \vdots \\ \displaystyle\int_0^{2\pi}\!\!\int_0^{2\pi} [G\mathrm{e}^{\mathrm{i}(-M\theta-M\tau)}]_{r=\rho=R}\,\mathrm{d}\theta\,\mathrm{d}\tau & \cdots & \displaystyle\int_0^{2\pi}\!\!\int_0^{2\pi} [G\mathrm{e}^{\mathrm{i}(M\theta-M\tau)}]_{r=\rho=R}\,\mathrm{d}\theta\,\mathrm{d}\tau \end{pmatrix},$$

and $\widetilde{\mathscr{G}}$ is identically defined but with the radial derivative $\partial_r G$ replacing G. By using Graf's addition theorem for Bessel functions it is possible to calculate explicit expressions for these matrix entries in a similar fashion to that used for the entries of the vector $\mathbf{f}_I$. However, it turns out that these expressions are numerically impracticable and we instead employ numerical techniques to evaluate the integrals appearing in $\mathscr{G}$ and $\widetilde{\mathscr{G}}$.

Calculation of these integrals proves to be the most numerically intensive facet of the solution process. It is therefore important to understand the difficulty in performing this task so that we may curtail the cost. A term-by-term numerical integration of the Green's functions in the series form given in equation (4.1) would incur numerical expense due to the slow convergence that ensues from the logarithmic singularity in G at the point $(x,y) = (\xi,\eta)$ (see below).

In order to minimise the number of numerical integrations that must be performed, we employ a method in which we subtract the singular part of the Green's function in the form of a simplified series, and add it back again as the closed form of this series. This technique is known as a Kummer transformation (see Nicorovici et al., 1994; Linton, 1998) and we proceed as follows. Let the matrix of Green's functions G of equation (4.1) be given by

$$G = \sum_{m=-\infty}^{\infty} S_m, \quad S_m = \frac{1}{4\mathrm{i}y_0} V_m^{-1} \mathrm{e}^{\mathrm{i}V_m|X|} \mathrm{e}^{-\mathrm{i}u_m Y},$$

and note that the series diverges logarithmically at the point $(x,y) = (\xi,\eta)$. We define the terms

$$t_{m,\pm} = \frac{1}{4m\pi} \mathrm{e}^{-(\pm u_0 + pm)|X| - \mathrm{i}(u_0 \pm pm)Y}, \quad p = \pi/y_0$$

for $m = 1, \ldots$, so that $S_{\pm m} \sim t_{m,\pm} I$ as $m \to \infty$, and at $(x,y) = (\xi,\eta)$ it is easily shown that $S_{\pm m} - t_{m,\pm} I \sim \mathrm{O}(m^{-2})$. By summing the series $\sum_{m=1}^{\infty}\{t_{m,-} + t_{m,+}\}$, we are able to rewrite G as

$$G = S_0 + \sum_{m=1}^{\infty} \{S_{\pm m} - t_{m,\pm} I\} + \frac{\mathrm{e}^{-\mathrm{i}u_0 Y}}{4\pi} \{\cosh\{u_0|X|\} \ln(q_- q_+) + \sinh\{u_0|X|\} \ln(q_-/q_+)\} I, \tag{4.17}$$

where the functions $q_\pm = q_\pm(X,Y)$ are defined by $q_\pm = 1 - \mathrm{e}^{-p(|X|\pm iY)}$. The latter representation of G given in equation (4.17) comprises the sum of a series that is convergent at all points and a function in closed form. We can now explicitly locate the logarithmic singularity in the term $\ln(q_- q_+)$ and perform the integration of the singularity contained within this function analytically. The value of this integral is given in Bennetts and Squire (2008).

A similar expression to our revised form of the matrix of Green's functions given above must also be found for its radial derivative. This is achieved by simply taking the derivative of G with respect to r from equation (4.17), and upon suitable rearrangement results in

$$\partial_r G = \widetilde{S}_0 + \sum_{m=1}^{\infty} \{\widetilde{S}_{\pm m} - \widetilde{t}_{m,\pm} I\} + \mathrm{sgn}(X) \frac{\mathrm{e}^{-\mathrm{i}u_0 Y}}{2y_0 q_- q_+} \{q_0 \cosh(u_0|X|) + \mathrm{i}q_1 \sinh(u_0|X|)\} \mathrm{e}^{-p|X|}. \quad (4.18)$$

In the above, the matrix terms $\widetilde{S}_m$ are defined as

$$\widetilde{S}_m = \frac{1}{4y_0} (\mathrm{sgn}(X)\cos(\theta) I - u_m \sin(\theta) V_m^{-1}) \mathrm{e}^{\mathrm{i}V_m|X|} \mathrm{e}^{-\mathrm{i}u_m Y} \quad (m = 1, \ldots),$$

and the scalar terms $\tilde{t}_{m,\pm}$ are

$$\tilde{t}_{m,\pm} = \mathrm{sgn}(X) \frac{1}{4y_0} \mathrm{e}^{\mp \mathrm{sgn}(X)\mathrm{i}\theta} \mathrm{e}^{-(\pm u_0 + pm)|X| - \mathrm{i}(u_0 \pm pm)Y} \quad (m = 1, \ldots).$$

It can be shown that $\widetilde{S}_{\pm m} - \widetilde{t}_{m,\pm} \sim \mathrm{O}(m^{-2})$ at $(x,y) = (\xi,\eta)$, which means that the series in equation (4.18) converges at all points. The terms q_0 and q_1 are given by

$$q_0 = \cos(pY - \mathrm{sgn}(X)\theta) - \mathrm{e}^{-p|X|}\cos(\theta), \quad q_1 = \sin(pY - \mathrm{sgn}(X)\theta) + \mathrm{sgn}(X)\mathrm{e}^{-p|X|}\sin(\theta).$$

Using a result that was proved in Bennetts and Squire (2008) it can be shown that as $(x,y) \to (\xi,\eta)$ along Γ (that is as $\theta \to \tau$ and $r = \rho = R$)

$$\frac{q_0 \cosh(u_0|X|) + \mathrm{i}q_1 \sinh(u_0|X|)}{q_- q_+} \to \frac{1}{2Rp} (\mathrm{sgn}(X) - Rp\cos(\theta)) - \mathrm{i}\frac{u_0}{p}\sin(\theta),$$

which is bounded. Hence, the function $\partial_r G$ has no singular points as it traverses the edge of the floe.

The series incorporated in the expressions (4.17) and (4.18) may then be evaluated at all points for the purpose of numerical integration, and all bounded closed functions are also numerically integrated. However, the series may still be slowly convergent around the point $(x,y) = (\xi,\eta)$, especially for larger values of u_0 and k_n. Therefore, we make use of higher-order Kummer transformations in a neighbourhood of this point in which the above series are replaced, for the purposes of numerical integration, by more rapidly convergent series and bounded polylogarithmic functions. Detailed explanations of how this is achieved may be found in Nicorovici et al. (1994) and Linton (1998).

Finally, in our evaluation of the integrals involved in the matrices $\mathscr{G}$ and $\widetilde{\mathscr{G}}$, we note the symmetries

$$\int_0^{2\pi}\int_0^{2\pi} [G\mathrm{e}^{\mathrm{i}(n\theta - m\tau)}]_{r=\rho=R} \,\mathrm{d}\theta\,\mathrm{d}\tau = \int_0^{2\pi}\int_0^{2\pi} [G\mathrm{e}^{\mathrm{i}(m\theta - n\tau)}]_{r=\rho=R} \,\mathrm{d}\theta\,\mathrm{d}\tau,$$

$$\int_0^{2\pi}\int_0^{2\pi} [G\mathrm{e}^{\mathrm{i}(n\theta - m\tau)}]_{r=\rho=R} \,\mathrm{d}\theta\,\mathrm{d}\tau = (-1)^{n+m} \int_0^{2\pi}\int_0^{2\pi} [G\mathrm{e}^{\mathrm{i}(-n\theta + m\tau)}]_{r=\rho=R} \,\mathrm{d}\theta\,\mathrm{d}\tau,$$

and

$$\int_0^{2\pi}\int_0^{2\pi}[(\partial_r G)\mathrm{e}^{\mathrm{i}(n\theta-m\tau)}]_{r=\rho=R}\,\mathrm{d}\theta\,\mathrm{d}\tau=(-1)^{n+m}\int_0^{2\pi}\int_0^{2\pi}[(\partial_r G)\mathrm{e}^{\mathrm{i}(-n\theta+m\tau)}]_{r=\rho=R}\,\mathrm{d}\theta\,\mathrm{d}\tau.$$

These relations extend to matrices the scalar versions given in Bennetts and Squire (2008).

Note that, unlike equation (4.14), the matrix system (4.15) is not diagonal and therefore couples the Fourier modes. Having calculated the entries of the vector of integrals of the incident wave, $\mathbf{f}_I$, and the matrices of integrals of the Green's functions and its radial derivative, $\mathscr{G}$ and $\widetilde{\mathscr{G}}$, it is now possible to solve for the vectors of unknowns $\mathbf{f}_0$ and $\mathbf{f}_1$. To do this we use (4.15) to express $\mathbf{f}_1$ in terms of $\mathbf{f}_I$ and $\mathbf{f}_0$, with

$$\mathbf{f}_1=\mathscr{G}^{-1}\Big(\frac{1}{2R}I+\widetilde{\mathscr{G}}\Big)\mathbf{f}_0-\frac{1}{R}\mathscr{G}^{-1}\mathbf{f}_I. \tag{4.19}$$

Using (4.19) to eliminate $\mathbf{f}_1$ from (4.14) leaves the system of $(2M+1)(N+1)$ equations

$$\Big(\frac{1}{2R}\mathscr{M}\mathscr{G}^{-1}+\mathscr{M}\mathscr{G}^{-1}\widetilde{\mathscr{G}}-I\Big)\mathbf{f}_0=\frac{1}{R}\mathscr{M}\mathscr{G}^{-1}\mathbf{f}_I, \tag{4.20}$$

in the $(2M+1)(N+1)$ unknowns contained in the vector $\mathbf{f}_0$, with the known forcing vector $\mathbf{f}_I$.

Using equation (4.20) we may calculate the vector $\mathbf{f}_0$ by means of an inversion of the $(2M+1)(N+1)$-dimensional matrix on the left-hand side. We then obtain $\mathbf{f}_1$ directly via equation (4.19), which provides us with the information needed to define the solution in the ice-covered region fully using the expressions given in equation (4.13).

As we described at the end of §4.1, we split our calculation of the free-surface velocity potential into the two régimes, defined by $|\xi|<R$ and $|\xi|\geqslant R$. For the latter we have the representation (4.4), which is in terms of reflection and transmission coefficients that may now be explicitly calculated using equation (4.16a–b). When $|\xi|<R$ we must use our calculated Fourier series representations of Φ and $\partial_r\Phi$ in the integral representation (4.3a), and all integrations are performed numerically using the Kummer transformations described in this section.

4.4 *The Scattering Matrix*

Quantities of particular interest are the amplitudes of the propagating waves scattered by the array. Recall that the number of propagating waves that exist in each particular problem depends on the number of real $\nu_{0,s}$, for which we have defined the set $S=\{s:\nu_{0,s}\in\mathbb{R}\}\equiv\{a,\ldots,b\}$. The size of this set depends on the free-surface wavenumber k_0, the width of the channel, $2y_0$, and the chosen value $u_0\in(-k_0,k_0)$ that defines the incident angle. Subsequently, the values u_s $(s\in S)$ define the angles at which the waves propagate towards/away from the floe with respect to the x-axis. Therefore, for each geometrical configuration, there are a finite number of scattered waves that travel at well-defined angles with respect to the Cartesian frame, and these are the waves that persist in the far-field.

For the purposes of this section we will consider a more general incident wave-field that is comprised of waves propagating at all of the available angles for the particular problem and from both $x\to\pm\infty$, so that

$$\Phi^I(x,y)=\sum_{s\in S}\{I_{s+}\tilde{\Phi}^I_{s+}(x,y)+I_{s-}\tilde{\Phi}^I_{s-}(x,y)\},\quad \tilde{\Phi}^I_{s\pm}(x,y)=(\mathrm{e}^{\mathrm{i}(\pm\nu_{0,s}x+u_s y)},0,\ldots,0)^T,$$

where $I_{s\pm}$ are the incident amplitudes and we have added the tilde to the functions to avoid confusion between the expansion into Fourier modes made in the previous section. The solution in the free-surface

fluid region may then similarly be decoupled into its response to each of the individual incident waves, and we write

$$\Phi(x,y) = \sum_{s\in S}\{I_{s+}\tilde{\Phi}_{s+}(x,y) + I_{s-}\tilde{\Phi}_{s-}(x,y)\}. \tag{4.21}$$

The far-field response of each $\tilde{\Phi}_{j\pm} = (\tilde{\phi}_{0,j\pm},\ldots,\tilde{\phi}_{N,j\pm})^T$ $(j \in S)$ is defined as

$$\tilde{\phi}_{0,j+}(x,y) \sim \begin{cases} \{\mathrm{e}^{\mathrm{i}(\nu_{0,j}x+u_jy)} + \sum_{s\in S} R^{(+)}_{j,s}\mathrm{e}^{\mathrm{i}(-\nu_{0,s}x+u_sy)}\} & (x\to-\infty), \\ \sum_{s\in S} T^{(+)}_{j,s}\mathrm{e}^{\mathrm{i}(\nu_{0,s}x+u_sy)} & (x\to\infty), \end{cases}$$

$$\tilde{\phi}_{0,j-}(x,y) \sim \begin{cases} \sum_{s\in S} T^{(-)}_{j,s}\mathrm{e}^{\mathrm{i}(-\nu_{0,s}x+u_sy)} & (x\to-\infty), \\ \mathrm{e}^{\mathrm{i}(-\nu_{0,j}x+u_jy)} + \sum_{s\in S} R^{(-)}_{j,s}\mathrm{e}^{\mathrm{i}(\nu_{0,s}x+u_sy)} & (x\to\infty), \end{cases}$$

and $\tilde{\phi}_{n,j\pm} \sim 0$ as $x\to\pm\infty$ $(n = 1,\ldots,N)$. The reflection coefficients $R^{(\pm)}_{j,s}$ and transmission coefficients $T^{(\pm)}_{j,s}$ may be calculated using equations (4.16a–b).

We can describe the relationship between the incident amplitudes and the scattered amplitudes through the scattering matrix $\mathfrak{S}$, which is defined by

$$\mathbf{B} = \mathfrak{S}\mathbf{I}_0, \quad \mathfrak{S} = \begin{pmatrix} R_+ & T_- \\ T_+ & R_- \end{pmatrix}, \quad \left.\begin{matrix} \{R_\pm\}_{j-a+1,i-a+1} = R^{(\pm)}_{j,i}, \\ \{T_\pm\}_{j-a+1,i-a+1} = T^{(\pm)}_{j,i}, \end{matrix}\right\} (i,j\in S)$$

where $\mathbf{I}_0 = (I_{a+},\ldots,I_{b+},I_{a-},\ldots,I_{b-})^T$ is the vector of incident amplitudes and $\mathbf{B} = (B_{a+},\ldots,B_{b+}, B_{a-},\ldots,B_{b-})^T$ is the vector of scattered amplitudes.

Certain properties of the scattering matrix may be deduced as follows. Consider the inner-products

$$\iint_{\Omega/\mathscr{D}} \{\tilde{\Phi}_i^T A_- \nabla^2\overline{\tilde{\Phi}}_j - (\nabla^2\tilde{\Phi}_i)^T A_-\overline{\tilde{\Phi}}_j\}\,\mathrm{d}x\,\mathrm{d}y,$$

for $i,j = a\pm,b\pm$. It is clear from the definitions (4.21) that each of the functions $\tilde{\Phi}_{m\pm}$ satisfies the differential system (3.4) and transition conditions (3.8). Applying Green's identity (4.2) to these inner-products and noting that A_- is a real, diagonal matrix we deduce that

$$\left.\begin{matrix} \sum_{s\in S}\nu_{0,s}\{R^{(\pm)}_{i,s}\overline{R}^{(\pm)}_{j,s} + T^{(\pm)}_{i,s}\overline{T}^{(\pm)}_{j,s}\} = \nu_{0,j}\delta_{i,j} + I_{i\pm,j\pm} \\ \sum_{s\in S}\nu_{0,s}\{R^{(\pm)}_{i,s}\overline{R}^{(\mp)}_{j,s} + T^{(\pm)}_{i,s}\overline{T}^{(\mp)}_{j,s}\} = I_{i\pm,j\mp} \end{matrix}\right\} (i,j\in S), \tag{4.22}$$

and

$$I_{i,j} = R\int_0^{2\pi}\{\tilde{\Phi}_i^T A_-(\partial_r\overline{\tilde{\Phi}}_j) - (A_-\partial_r\tilde{\Phi}_i)^T\overline{\tilde{\Phi}}_j\}_{r=R}\,\mathrm{d}\theta \quad (i,j = a\pm,\ldots,b\pm).$$

As they stand, the identities (4.22) tell us nothing due to the presence of the terms $I_{i,j}$. However, for each solution in the free-surface domain, $\tilde{\Phi}_{s\pm}$ $(s\in S)$, there is an associated velocity potential vector $\tilde{\Psi}_{s\pm}$ in the ice-covered domain defined analogously to (4.21), where the vectors $\tilde{\Phi}_{s\pm}$ and $\tilde{\Psi}_{s\pm}$ are linked

through the jump conditions (4.12). We may therefore rewrite $I_{i,j}$ in terms of the solutions in the ice-covered domain, so that

$$I_{i,j} \quad = \quad R\int_0^{2\pi}\left\{\tilde{\Psi}_i^T A\partial_r\overline{\tilde{\Psi}}_j - (\partial_r\tilde{\Psi}_i)^T A\overline{\tilde{\Psi}}_j + \tilde{\Psi}_i^T\widetilde{D}\overline{\tilde{\Psi}}_j\right\}_{r=R}\mathrm{d}\theta,$$

in which we have used the symmetry of A and the property $Q-Q^T=\widetilde{D}$. Now, consider the inner-products of the functions $\tilde{\Psi}_i$ and $\tilde{\Psi}_j$ $(i,j\in S)$

$$\iint_{\mathscr{D}}\{\tilde{\Psi}_i^T A\nabla^2\overline{\tilde{\Psi}}_j - (A\nabla^2\tilde{\Psi}_i)^T\overline{\tilde{\Psi}}_j\}\,\mathrm{d}x\mathrm{d}y \tag{4.23a}$$

and of their respective displacements $\tilde{w}_i^{(p)}$ and $\tilde{w}_j^{(p)}$ $(p=1,2)$,

$$\iint_{\mathscr{D}}\{(\tilde{w}_i^{(1)}\nabla^2\overline{\tilde{w}}_j^{(2)} - \overline{\tilde{w}}_j^{(1)}\nabla^2\tilde{w}_i^{(2)}) + (\tilde{w}_i^{(2)}\nabla^2\overline{\tilde{w}}_j^{(1)} - \overline{\tilde{w}}_j^{(2)}\nabla^2\tilde{w}_i^{(1)})\}\,\mathrm{d}x\mathrm{d}y. \tag{4.23b}$$

Manipulations of equations (4.23a–b) involving the relationships $\{\tilde{D}\}_{j,i}=-\{\tilde{D}\}_{i,j}$ and $\partial_r\{\tilde{D}\}_{j,i}=\{B\}_{j,i}-\{B\}_{i,j}$, and Green's identity (4.2), followed by integration by parts, and imposition of the bending moment and shearing stress conditions (2.2a–b) on the resulting boundary integrals may be used to show that $I_{i,j}=0$ in the case of axisymmetric geometry.

The simplified versions of identities (4.22) are analogous to those given by Porter and Porter (2001) for free-surface flows over three-dimensional periodic topography. As such we see that the relationship that these authors derived for the scattering matrix in their problem also holds for the scattering matrix $\mathfrak{S}$ here, namely

$$\hat{\mathfrak{S}}^*\hat{\mathfrak{S}}=\hat{\mathfrak{S}}\hat{\mathfrak{S}}^*=I,\quad \hat{\mathfrak{S}}=\mathscr{V}^{1/2}\mathfrak{S}\mathscr{V}^{-1/2},\quad \mathscr{V}=\mathrm{diag}\{v_{0,a},\ldots,v_{0,b},v_{0,a},\ldots,v_{0,b}\}, \tag{4.24}$$

where $\mathfrak{S}^*=\overline{\mathfrak{S}}^T$ denotes the Hermitian transpose of the scattering matrix. Consequently, we also have that $|\det(\mathfrak{S})|=1$.

Inherent in the first of the relations (4.22) is the conservation of energy condition identity

$$\sum_{s\in S}v_{0,s}\{|R^{\pm}_{s,j}|^2+|T^{\pm}_{s,j}|^2\}=v_{0,j}\quad(j\in S). \tag{4.25}$$

(cf. Achenbach et al., 1988). As noted in Porter and Porter (2001) this implies that energy conservation is an intrinsic property of the MMA and therefore only an indication that our calculated approximation is valid rather than a gauge of its accuracy.

Other observations made by Porter and Porter for the scattering matrix in their free-surface problem may be reinterpreted for the current case. Firstly, by noting the symmetry of the geometry in the y-axis we find the equality of the reflection and transmission coefficients $R_-=R_+$ and $T_-=T_+$. Similarly, by noting the symmetry of the geometry in the x-axis and using the result (4.24) we can show that $\mathfrak{S}^T=\mathscr{V}\mathfrak{S}\mathscr{V}^{-1}$, whence $\mathrm{diag}\{v_{0,a},\ldots,v_{0,b}\}R^T_{\pm}=\mathrm{diag}\{v_{0,a},\ldots,v_{0,b}\}R_{\pm}$ and $\mathrm{diag}\{v_{0,a},\ldots,v_{0,b}\}T^T_{\pm}=\mathrm{diag}\{v_{0,a},\ldots,v_{0,b}\}T_{\mp}$. One further result, which is that $\overline{\mathfrak{S}}_{\pm}\mathfrak{S}_{\pm}=I$, may be gleaned from Porter and Porter and uses the symmetry of the geometry in the x-axis.

5. Numerical Results

The results that are presented in this section will use truncations that ensure the solutions are converged and therefore represent the full-linear solution. That is, a sufficient number of vertical modes N (see

equation (3.1)), Fourier modes M (see equation (4.6)), and terms in the Green's functions (see equation (4.1)) have been used to perform calculations. We note that the dimensions of truncations required to gain a converged solution are problem specific. Specific mention of the values used will only be given when we feel that it is of benefit to the reader.

5.1 *Comparison with alternative interaction theory*

We have already noted that the problem of a periodic line array of floating elastic bodies has been solved by previous authors, namely Peter et al. (2006) and Wang et al. (2007). However, these authors used floes of different geometries to those that we deal with in this work. In particular, it was assumed that the thickness of the floes is constant and there is no submergence, so the method reported here is more general and physically accurate in this respect.

Authors Wang et al. combined the bodies in the array by means of a periodic Green's function, in a similar fashion to the method that is employed in this work. This contrasts with Peter et al. in which the interactions are calculated using Graf's formula, where the bodies may be taken to be of circular shape, with their individual response found using Peter et al. (2004) or Meylan (2002), for example. This method is markedly different from our own and its existence provides a stringent test of the accuracy of our results. Although we are restricted to floes of constant thickness and zero draught in this comparison due to the solution method of Peter et al., it is the calculation of their interaction through a matrix of Green's functions that is the predominant new feature of the present work, and its validity may be tested without the need for more complicated ice floe geometries.

In this section we display a selected set of results that compares the displacement of the floe in the central channel, as calculated using our own method, to that found using a combination of Peter et al. (2006, 2004). Specifically, figure 2 presents comparisons in the form of contour plots for three problems. The problems share the floe radius $R = 50\,\mathrm{m}$, constant ice thickness $D = 1\,\mathrm{m}$, floe separation $y_1 = 5\,\mathrm{m}$ and frequency $\omega = 1\,\mathrm{rad/s}$. These values have been chosen so that sufficient scattering is occurring to make this a valid test case and the results that we present here are indicative of a wide range of situations investigated. The angle at which the incident wave propagates towards the array (with respect to the x-axis) changes between the subfigures, with the chosen values being $\hat{\theta} = 0$, $\pi/6$ and $\pi/3$. As the angle of incidence increases more terms in the Green's functions are required to maintain accuracy.

The similarity between the results calculated using our method and those of Peter et al., both qualitatively and quantitatively, is excellent and it is clear that we are generating the same solutions. This is true even in the case of incident angle $\pi/3$, where the interaction of the floes is particularly strong. The small discrepancies that are visible are mainly confined to the vicinity of the edge of the floe, which is predictable, as at these points the flexure is greatest. For two such fundamentally different approaches to the calculation of the interaction of floating bodies in an infinite array, the agreement that we find here is extremely encouraging.

5.2 *The effects of floe spacing*

Let us now examine how the space between the floes in the array affects the displacement they experience. To begin with in this section we will continue to use floes of radius $R = 50\,\mathrm{m}$ and zero draught, and will vary their (constant) thickness, the frequency and the angle of incidence, in addition to the floe spacing. Results for the corresponding solitary floe, which are calculated using the method outlined in Bennetts et al. (2009b), are also given. For all of the parameter values that were tested it was found that the results of the single-line array tend to those of the solitary floe as the spacing is increased and this

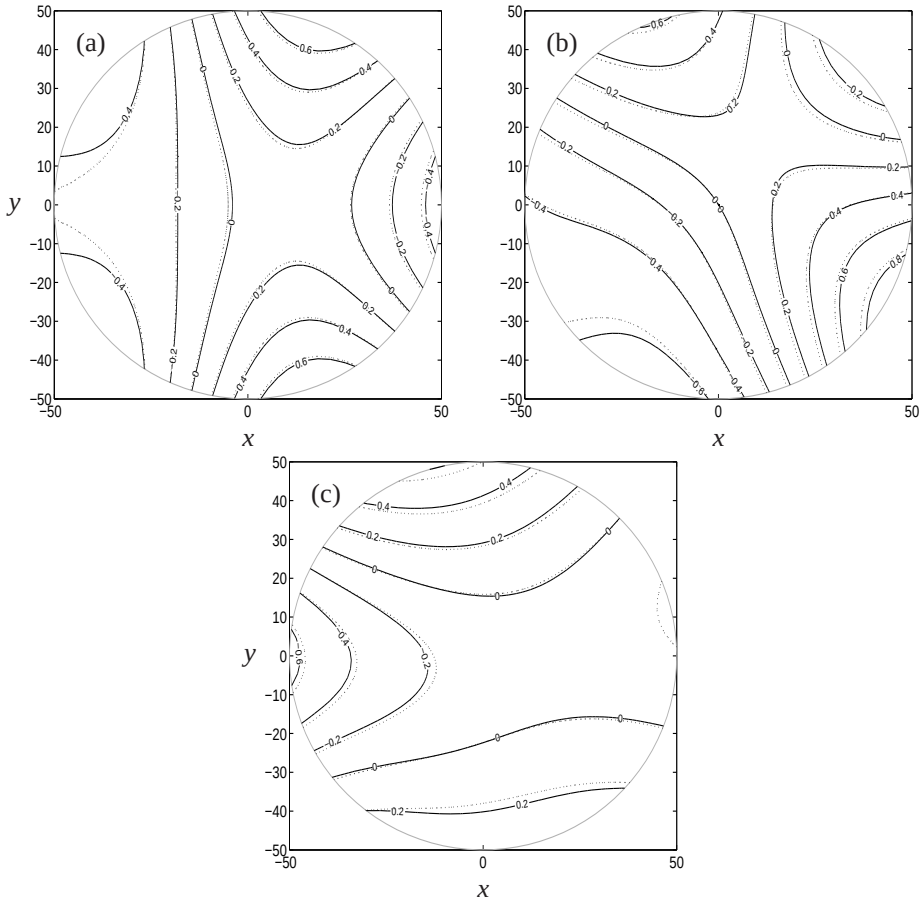

FIG. 2. Comparison to the Graf's formula interaction theory of Peter et al.. Each subfigure is a contour plot that displays the displacement of the floe for a particular problem. The values of the displacement are overlain on each subfigure (in metres). In all problems the floes are of radius $R = 50\,\mathrm{m}$, constant thickness $D = 1\,\mathrm{m}$, zero draught $d = 0$, and have a $y_1 = 5\,\mathrm{m}$ separation from the adjacent floe in the array. The incident wave propagates at an angle: part (a) 0, (b) $\pi/6$, and (c) $\pi/3$, with respect to the $x-$axis. Results using the theory outlined in this work are shown with solid lines, with corresponding results calculated by Peter et al. shown with dotted lines. The perimeter of the floe is displayed by the grey circle.

provides further evidence that our interaction theory is accurate.

Figures 3–6 show the displacement of the floe that lies in the channel Ω along the contour $y = 0$ at the instant $t = 0$, that is $\Re\mathrm{e}(\eta)$. In each figure the same floe thickness and wave frequency are maintained, with the angle of incidence, as in the previous section, changing from $\hat{\theta} = 0$, to $\hat{\theta} = \pi/6$, to $\hat{\theta} = \pi/3$ between the subfigures. We show results for the two ice thicknesses $D = 0.5\,\mathrm{m}$ and $1\,\mathrm{m}$, and the two frequencies $\omega = 1\,\mathrm{rad/s}$ and $1.25\,\mathrm{rads/s}$. As the frequency and/or ice thickness increase it is necessary to use more vertical modes to achieve the same level of convergence, which is expected and consistent with previous studies (see Bennetts et al., 2007, for example). Each subfigure compares displacements for four different floe spacings, with the corresponding results for the solitary floe superimposed. We note that a wider channel allows for a more complicated structure in the y-direction and hence more

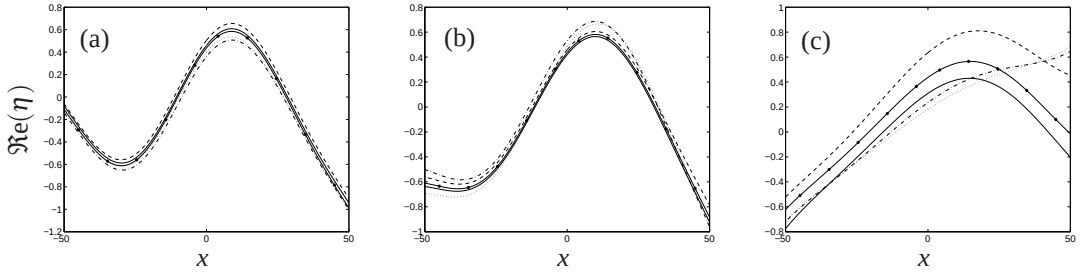

FIG. 3. A cross-section of the displacement of the floe that lies on the x-axis at an instant in time. The floes in the array are of radius $R = 50\,\mathrm{m}$, constant thickness $D = 0.5\,\mathrm{m}$ and zero draught $d = 0$. In each subfigure results are given for the spacings $y_1 = 5\,\mathrm{m}$ (dotted curves), 20 m (dot-dash), 100 m (dashed) and 400 m (solid), with the results for the solitary floe superimposed (solid curves with dots overlaid). The incident wave is of frequency $\omega = 1\,\mathrm{rad/s}$ and propagates at an angle: part (a) 0, (b) $\pi/6$, (c) $\pi/3$ with respect to the x-axis.

terms need to be used in the Green's functions.

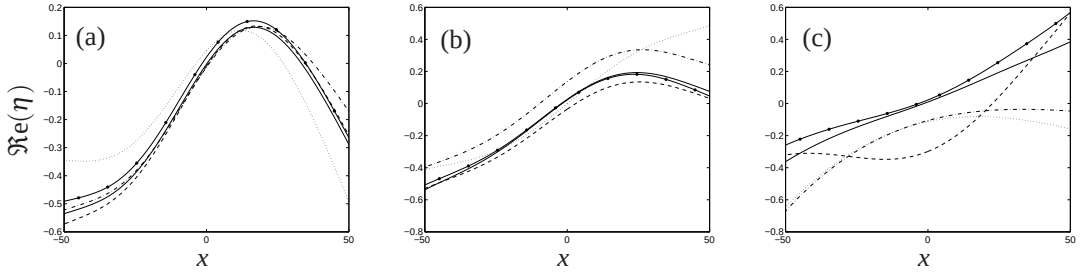

FIG. 4. As in fig. 3 but for floes of thickness $D = 1\,\mathrm{m}$.

In all cases we can again observe that, as the spacing increases and the interactions of the floes die out, the displacements tend to that of the corresponding solitary floe. However, the rate at which this occurs is dependent on the properties of the incident wave, and those of the array and the floes that constitute it. For instance, we see that in some cases the interactions of the floes persist for larger separations with the thicker floes, which may be attributed to the ice edge providing a stronger barrier to the incident wave and hence generating more significant waves between the floes (see the results for $\omega = 1\,\mathrm{rad/s}$, figures 3–4). Conversely, for the same reason the thicker floes tend to experience less displacement and may appear to be less responsive to changes in floe separations (see the results for $\omega = 1.25\,\mathrm{rads/s}$, figures 5–6).

At the higher frequency, $\omega = 1\,\mathrm{rad/s}$, we find that interactions remain evident for the larger spacings. This is unsurprising as shorter waves are reflected more strongly by the floes, and also cause greater activation of the evanescent waves. Furthermore, there is more scope for the appearance of waves propagating away from the array at angles other than that of the incident wave at higher frequencies. They therefore lead to more complicated and more sustained floe couplings.

The dominant factor that determines the amount of interaction between the floes in these figures is the angle at which the incident wave propagates towards the array. For a normally incident wave almost no interaction occurs beyond $y_1 = 20\,\mathrm{m}$, with the results for $y_1 = 5\,\mathrm{m}$, although distinguishable, similar both quantitatively and qualitatively to those of the solitary floe. By changing to the oblique incidence of

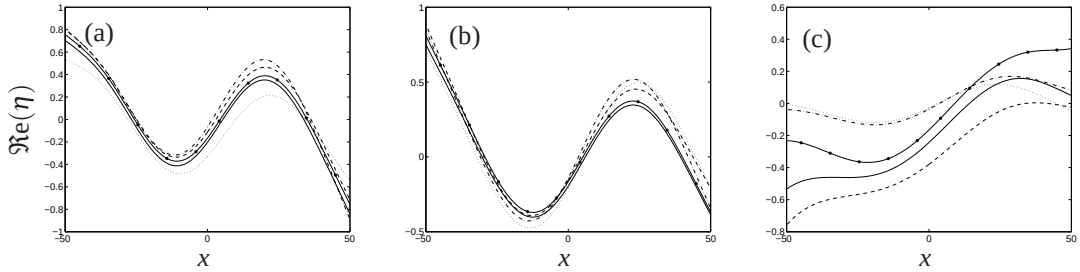

FIG. 5. As in fig. 3 but for a frequency $\omega = 1.25\,\mathrm{rads/s}$.

$\pi/6$, we do little to change this behaviour, with only the displacement for the 5 m separation, frequency $\omega = 1\,\mathrm{rad/s}$ and ice thickness 1 m displaying noticeably different properties to its counterparts.

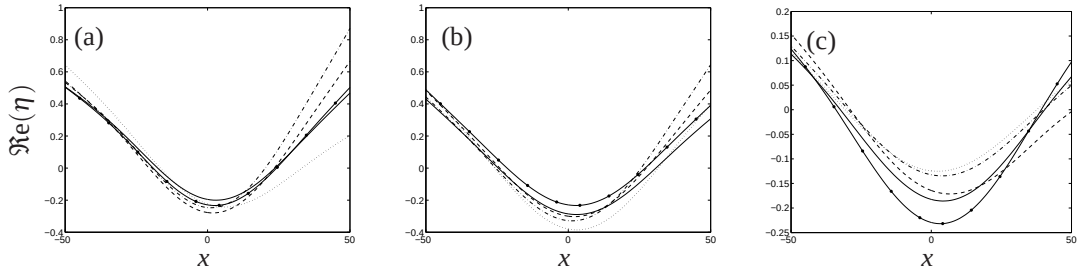

FIG. 6. As in fig. 4 but for a frequency $\omega = 1.25\,\mathrm{rads/s}$.

When the angle is increased to $\pi/3$ the effects of the array become apparent. In all cases the presence of the periodic geometry now clearly distinguishes the displacement shown by the floes in the array from that of the solitary floe, even for the 400 m spacing. For this incident angle the flexural response of the floes in the closely spaced arrays can bear quite different characteristics to the solitary floe. This is particularly visible for the $D = 1\,\mathrm{m}$, $\omega = 1\,\mathrm{rad/s}$ case with the floe separations $y_1 = 5\,\mathrm{m}$ and 20 m. We therefore conclude that, for these typical geometries, a significant angle of incidence is necessary for the interaction of the floes in the array to be evident in the flexure of the floes.

We now turn our attention to the influence of the floe spacing on the far-field structure of the solution. As such, in figure 7 we plot the reflection coefficients of the propagating waves over the interval 5–15 s of wave periods ($2\pi/\omega$) for floes of thickness $D = 0.25\,\mathrm{m}$, radius $R = 10\,\mathrm{m}$ and zero draught. The subfigures then move between the floe spacings $y_1 = 1\,\mathrm{m}$, 5 m, 10 m and 20 m. We note that for these smaller floes, as compared to the radius $R = 50\,\mathrm{m}$ used previously, a significantly smaller number of Fourier modes are required to gain sufficient convergence of the solution.

Recall that, due to the periodic geometry being studied, it is possible for more than one propagating wave to be reflected by the array, with wavenumbers (and hence oblique angles) determined by the quantities $v_{0,s}$ and u_s ($s \in S$). For the geometry used in figure 7, the chosen angle of incidence $\hat{\theta} = \pi/3$ and the chosen interval of frequencies, only one extra propagating wave is generated other than the primary reflected wave. This is the wave related to the reflection coefficient $R_{0,-1}$, and only exists for

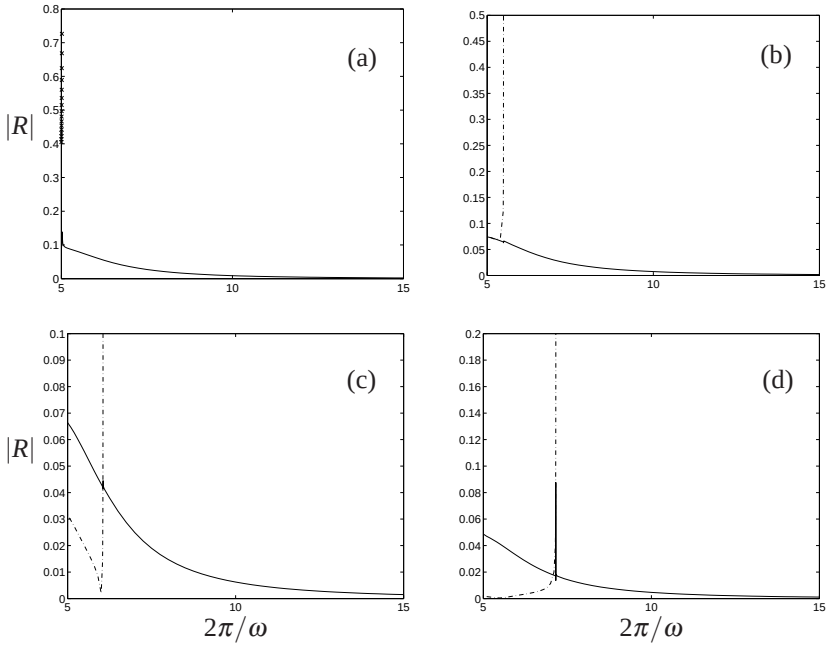

FIG. 7. The modulus of the reflection coefficients, $|R_0|$ (solid lines) and $|R_{-1}|$ (broken lines or crosses), as continuous functions of wave period, for an incident angle of $\pi/3$. The floes are of radius $R = 10\,\mathrm{m}$, constant thickness $D = 0.25\,\mathrm{m}$ and zero draught. The floe spacing changes between the subfigures, with: part (a) $y_1 = 1\,\mathrm{m}$, (b) $y_1 = 5\,\mathrm{m}$, (c) $y_1 = 10\,\mathrm{m}$, and (d) $y_1 = 20\,\mathrm{m}$.

periods small enough to ensure that

$$k_0 \geqslant \frac{\pi}{y_0(\sin\frac{\pi}{3}+1)}. \tag{5.1}$$

At the period at which this wave 'cuts-in', $v_{0,-1} = 0$ and $u_{-1} = k_0$, which describes a resonant wave that propagates parallel to the array and no solution is available using our method. As we draw near to such a period we find that results become more expensive to calculate due to larger truncations being required to achieve convergence. Despite this we are able to produce accurate results for points extremely close to the resonant frequency and thus determine the nature of the solution in its vicinity. As the period decreases further the secondary wave reflects away from the array at an increasing angle that approaches the direction of the primary reflected wave asymptotically as the period tends to zero.

The primary reflected wave is related to the reflection coefficient $R_{0,0}$ and is present for all periods. It is clear from the inequality (5.1) that, as the floe separation is increased, the secondary propagating wave will continue to exist for larger periods, and this feature is evident in the plots. In fact, as the secondary wave only exists for such a small interval of the wave periods shown on this figure, we found it necessary to use crosses so that it may be detected. For simplicity, from now on in our figures and discussion, we relabel the coefficients of the propagating waves as $R_j \equiv R_{0,j}$ $(j \in S)$.

The curves that denote the reflected coefficient of the primary wave are smooth and monotonic over virtually the entire spectrum of periods in the problems considered here. However, at the periods at which a supplementary propagating wave cuts-in, they do appear to experience 'spiky' behaviour. This is consistent with other studies involving periodic arrays, for example Linton and Evans (1993), and these authors used an argument based on the energy conservation (4.25) and numerical results to

provide strong evidence that the scattered amplitudes are in fact continuous as they pass through these resonant points. We therefore infer that the $|R_0|$-curves are just non-smooth rather than discontinuous when $|R_{-1}|$ cuts-in.

Results for the reflection coefficient of the secondary wave are less predictable. For the spacings $y_1 = 5\,\mathrm{m}$ and $10\,\mathrm{m}$, there is a local minimum present in this quantity, with $|R_{-1}| \approx 0$ in the case of $10\,\mathrm{m}$ spacing. Although the amplitude of the secondary wave is generally less than that of the primary wave, as we approach the 'cut-off' point for the secondary wave, its amplitude rises rapidly, far exceeding that of the primary wave, and to a degree depending here on the spacing used. Growth of this quantity is unsurprising as we are approaching a resonant frequency. Also, it may be inferred that a reflected wave travelling nearly parallel to the array produces strong effects, particularly for the closely spaced $y_1 = 1\,\mathrm{m}$ array in which the amplitude of $|R_{-1}|$ is greatest.

5.3 *Thickness variations and submergence*

Up to this point we have only looked at results for arrays in which the constituent floes are of constant thickness and zero draught. However, our solution procedure allows for the inclusion of axisymmetric thickness variations and a physically realistic Archimedean draught. Thorough investigations of the incorporation of these new features into the model of a solitary floe, through the use of the MMA, have been made previously by Bennetts (2007) and Bennetts et al. (2009b). For this reason it is not necessary to conduct an extensive study of the effects of thickness variations and submergence, but it is still of interest to observe what influence their introduction has in the setting of the current geometry.

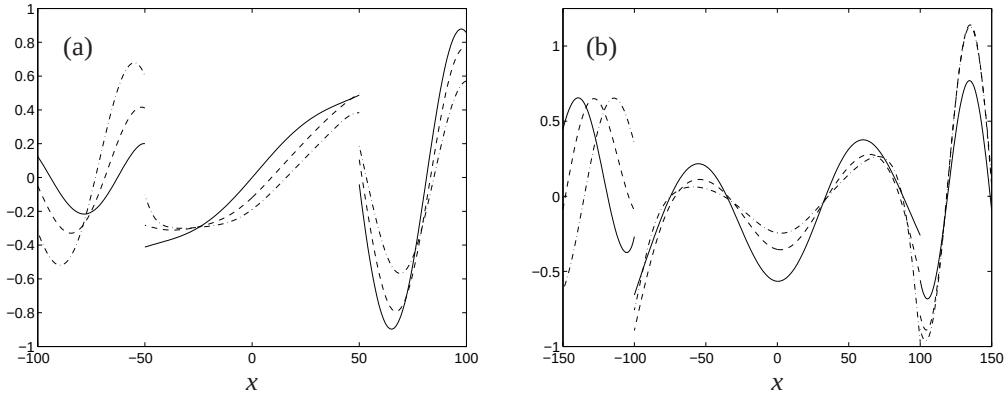

FIG. 8. A cross-section of the displacement of the floe along with the surrounding free-surface displacement (reflected $x < -R$, transmitted $x > R$) taken along the x-axis. The incident wave is of frequency $\omega = 1\,\mathrm{rad/s}$ and oblique angle $\pi/6$, and the floes are of radius: part (a) $R = 50\,\mathrm{m}$, (b) $R = 100\,\mathrm{m}$, and a $y_1 = 5\,\mathrm{m}$ separation. In each subfigure three separate results are shown for floes of differing thickness. The solid curves display the results for floes of constant thickness $D = 1\,\mathrm{m}$ and zero draught. The broken curves show results for floes that vary quadratically in thickness in the form of equation (5.2), with $D_0 = 0.5\,\mathrm{m}$, $l = 0.4\,\mathrm{m}$ and $u = 0.1\,\mathrm{m}$ (dashed curves), and $D_0 = 0.1\,\mathrm{m}$, $l = 0.7\,\mathrm{m}$ and $u = 0.2\,\mathrm{m}$ (dot-dash).

Figures 8–9 use four example problems to display the effects of introducing quadratic thickness variations of the form

$$D(r) = D_0 + \frac{u+l}{R}(R-r)^2; \quad d(r) = \frac{l}{R}(R-r)^2, \tag{5.2}$$

where D_0 is the edge thickness, u is the amplitude of the upper surface and l is the amplitude of the

lower surface. The figures show the displacement of the floes along the x-axis along with the scattered free-surface profile in a vicinity of the floe, which is calculated using the expression (4.4).

Each subfigure gives results for three different geometries, with one a constant floe of thickness $D = 1\,\mathrm{m}$ (solid curves), and two involving floes that increase in thickness quadratically from the edge of the floe to the centre (broken curves). Both of these floes have a thickness of 1 m at their centre ($r = 0$), with one having an edge thickness of 0.5 m (dotted curves) and the other 0.1 m (dot-dash). The variations are set so that the lower surface of the floe varies more rapidly than the upper surface. Results are shown for an oblique angle $\hat{\theta} = \pi/6$, the two frequencies $\omega = 1\,\mathrm{rad/s}$ and $\omega = 1.25\,\mathrm{rads/s}$, a floe separation of $y_1 = 5\,\mathrm{m}$ and the two floe radii $R = 50\,\mathrm{m}$ and $100\,\mathrm{m}$.

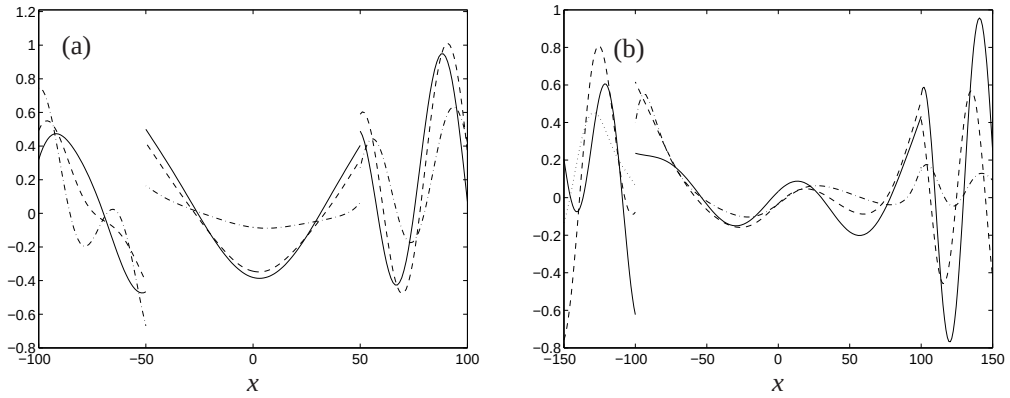

FIG. 9. As in fig.8 but for frequency $\omega = 1.25\,\mathrm{rads/s}$.

In all cases we see that the inclusion of thickness variations clearly distinguish the profile of the solution, especially in the more extreme $D_0 = 0.1\,\mathrm{m}$ case. However, the behaviour shown in these plots is complicated and it is difficult to ascertain exact implications of such changes to the floe geometry. We do note that there is a tendency for greater flexure of the floe at its edge when its thickness is thinner at this boundary. The same floes then damp the travelling wave more rapidly towards their centre. Conversely the displacement of the uniform floes is more evenly distributed.

As the flexure of larger floes is more complicated, it is unsurprising to see that the shape of the displacement varies to a larger degree in the $R = 100\,\mathrm{m}$ cases. It is also unsurprising to note that the magnitude of the displacement varies to a greater degree for the higher frequency $\omega = 1.25\,\mathrm{rads/s}$, as we expect the reflection caused by the different edge thicknesses to be exacerbated in this case.

Likewise, we note similar differences in the surrounding free-surface profile of the scattered waves. There is a tendency towards a larger amplitude transmitted wave when the floe is uniform, and correspondingly, a greater reflected amplitude when thickness variations are present. This would imply that in these cases, the impediment provided by the protruding portion of the floe is responsible for greater scattering than the thicker ice edge. The qualitative, as well as quantitative, differences of the waves alter with the changing floe shape for the frequency $\omega = 1.25\,\mathrm{rads/s}$, and this is particularly evident in the reflected wave when the radius is 50 m.

For the remainder of the results we will look at how the introduction of a realistic floe submergence affects the induced displacement by the incoming wave and the scattering produced in the free-surface domain. Here we will consider floes of a uniform $D = 1\,\mathrm{m}$ thickness, for which the Archimedean condition requires a $d = 0.9\,\mathrm{m}$ draught. It has previously been shown for a solitary floe (see Bennetts, 2007;

Bennetts et al., 2009b) that the introduction of edge submergence generally causes greater reflection and hence a smaller floe displacement at relatively short wavelengths but that this behaviour may be overridden by the fine structure found in the solutions, particularly for three-dimensional models. Here, we are concerned with how a physically correct draught affects the results within the context of our periodic structure, especially with respect to changes in the floe spacing and angle at which the incident wave propagates towards the array.

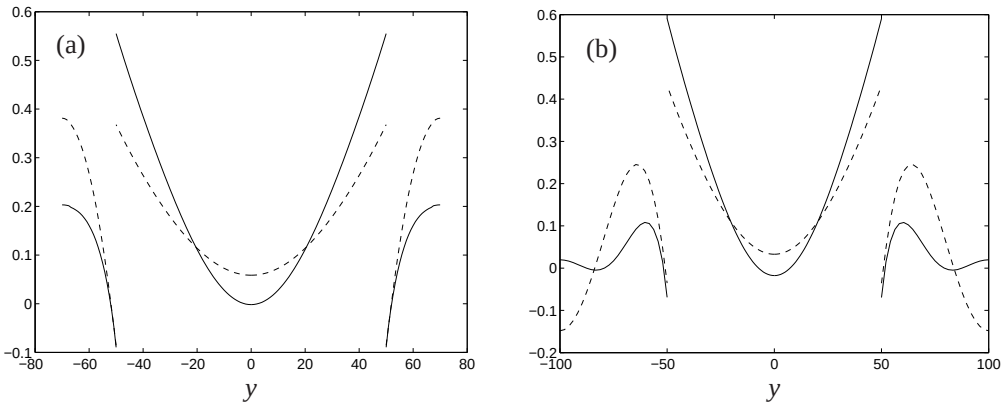

FIG. 10. Comparison of results for floes of zero draught (solid curves) against floes with Archimedean draught included (broken). Plots show cross-sections of the floe displacement along with the surrounding (scattered) free-surface displacement taken along the y-axis. The incident wave is of frequency $\omega = 1\,\mathrm{rad/s}$ and is normally incident. Floes are of radius $R = 50\,\mathrm{m}$, constant thickness $D = 1\,\mathrm{m}$, and separations: part(a) $y_1 = 40\,\mathrm{m}$, (b) $y_1 = 100\,\mathrm{m}$.

Figures 10–11 contain plots of the displacement of the floe in Ω along the y-axis together with the surrounding scattered free-surface profile for zero submergence (solid curves) and Archimedean draught (broken curves), for four different problems. In all of the problems the floes are of radius $R = 50\,\mathrm{m}$ and the frequency is $\omega = 1\,\mathrm{rad/s}$. The distance of separation changes from $y_1 = 40\,\mathrm{m}$ to $100\,\mathrm{m}$ between the subfigures, and the different figures show the cases in which the angle of incidence is normal ($\hat{\theta} = 0$) and $\hat{\theta} = \pi/6$. These choices are made in order that the surrounding free-surface takes up a non-trivial proportion of the y-axis but also, so that the interaction of the floes is worth investigating. Unlike the previous figures, here it is necessary to use the integral expression (4.3a) to calculate the surrounding free-surface profile as $\xi = 0 < R$.

In figure 10 the incoming wave is normally incident and we note that the displacement of the floes changes only marginally when the separation is varied, which is consistent with our earlier findings. As predicted, here the floes resist the incident wave, more so when they possess a submergence. Accordingly these floes are a greater source of scattering and we see that the amplitude of the surrounding waves increases when draught is included. It is unsurprising to note that the profiles of the scattered waves differ significantly when the distance between the floes changes, but also that there is a qualitative as well as quantitative difference between the waves scattered by the zero draught and Archimedean draught floes for the larger $y_1 = 100\,\mathrm{m}$ separation.

The incoming wave takes an angle of $\pi/6$ in figure 11. Although this leads to greater floe-floe interaction, which is evident in the change in the displacement of the floe when the separation distance is varied, the effects of the introduction of an Archimedean draught are now minimal in regard to both the floe displacement and the scattered wave profiles. This is, perhaps, surprising, and we will discuss

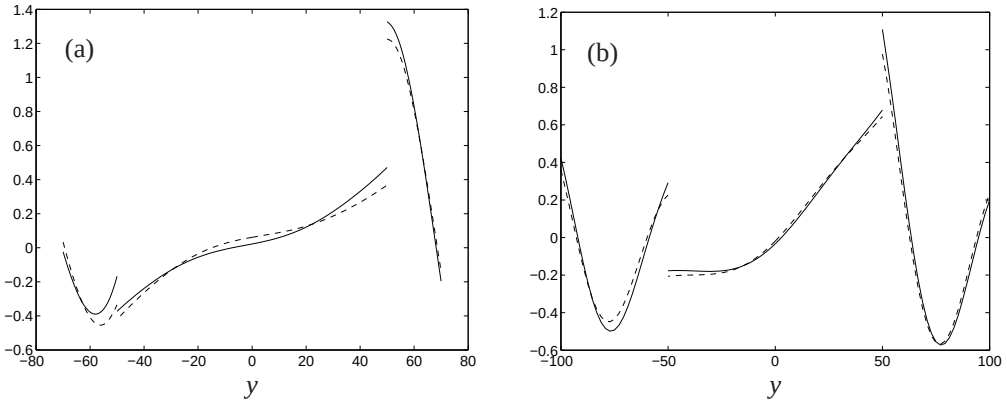

FIG. 11. As in fig.10 but for an incident angle of $\pi/6$.

this phenomenon further shortly. We also note that a greater proportion of the incident wave is scattered on the side from which it approaches the floe but that, as the distance between the floes increases and less floe interaction occurs, this feature diminishes.

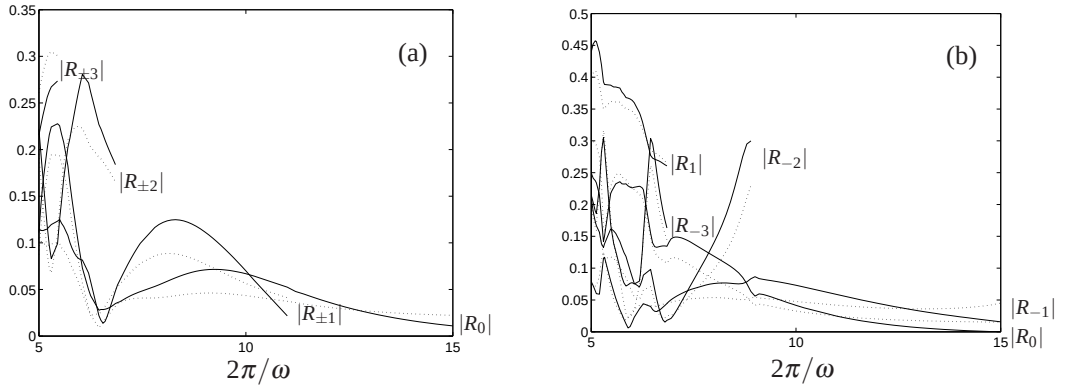

FIG. 12. The modulus of the reflection coefficients, $|R_j| \equiv |R_{0,s}|$ ($s \in S$), of the propagating waves as continuous functions of the wave period, for floes of radius $R = 50\,\mathrm{m}$ and constant thickness $D = 1\,\mathrm{m}$, comparing results for floes of zero draught $d = 0$ (solid curves) and an Archimedean draught $d = 0.9\,\mathrm{m}$ (broken). The floe spacing is $y_1 = 40\,\mathrm{m}$ and the incoming wave is: part (a) normally incident, and (b) $\pi/6$ obliquely incident.

Figure 12 displays the modulus of the reflection coefficients over the period interval 5–15 s, as in figure 7, but for a single separation distance and comparing results for zero draught floes and floes that include an Archimedean submergence. The geometry used is as in parts (a) of figures 10–11, and the incident angles correspond to these two figures respectively. Due to the larger floe radius and floe separation used here in relation to those of figure 7, a greater number of propagating waves are present in these plots. Also, as the floes are larger (with respect to the incident wavelengths) local extrema are apparent in these results. Thus the structure of the reflected amplitudes is more complicated in this case as opposed to the previous such figure.

We note that the overall number of propagating waves generated from both of the incident angles is

the same here. However, for clarity we have omitted $|R_{-4}|$ and $|R_{-5}|$ from part (b), which only appear for periods $\lessapprox 6\,\mathrm{s}$. It is not necessary to omit any curves for the case of normal incidence due to the symmetry $R_j = R_{-j}$. Irrespective of the extrema mentioned in the previous paragraph, the modulus of the reflection coefficients can appear quite rough over the smaller periods. This effect is due to the number of resonant frequencies, at which supplementary propagating waves cut-in/off, that are present for the geometry and incident waves considered here. As we noted in our discussion of figure 7, the reflection coefficients are not smooth around these points. However, unlike figure 7, here we do not fully resolve the spiky behaviour as it would be somewhat obstructive to the study of the introduction of submergence.

At most points in the spectrum of wave periods considered in this figure, the introduction of Archimedean draught clearly distinguishes its reflection coefficient from its zero-draught counterpart. The complicated structure of these quantities makes it difficult to draw implications about the changes that this additional feature causes. However, it is clear that the qualitative nature of the corresponding curves are similar, with extrema appearing for approximately the same period, although it is at these points at which the quantitative differences are most pronounced.

For the incident wave period when $\omega = 1\,\mathrm{rad/s}$, namely $2\pi\,\mathrm{s}$, we can relate the values of the reflection coefficients in figure 12 to the corresponding profiles shown in figures 10–11 parts (a). At this point the values of the corresponding Archimedean draught/zero draught reflection coefficients are distinct in the case of normal incidence. This contrasts to the case of oblique incidence for which the respective reflection coefficients are close, and is consistent with our findings for the profiles made earlier. We note though that this is just an isolated frequency/period, and that at other times the reflection coefficients for the obliquely incident wave may be further apart and those for the normally incident wave are closer together. Therefore, the similarity of the results shown in figure 11 cannot be taken as a generic property of obliquely incident waves, nor can the changes caused by the introduction of submergence for a normally incident wave shown in figure 10.

6. Conclusions

A solution method has been outlined for a geometrical configuration that consists of an infinite straight-line array of equally-spaced, identical ice floes in a fluid domain with a flat bed, which is forced by an obliquely incident wave. By use of a variational principle and an expansion of the vertical dependence of the unknown velocity potential, we defined a multi-mode approximation that is capable of reproducing the full-linear solution to an arbitrarily specified degree of accuracy. Using this method reduces our calculations to the horizontal plane only, and we are left to solve for vectors of unknown functions in the domains of the free-surface fluid and ice-covered fluid independently, with given jump conditions that relate these two solutions at their common boundary.

By implementing the periodicity of the solution, we were able to express the velocity potential in the free-surface domain, and thus capture the interactions of the floes, in terms of an integral around the edge of a single floe. The floes themselves were taken to be axisymmetric and we included thickness variations and a non-zero draught. This allowed us to reuse the solution procedure of Bennetts et al. (2009b), which we adjusted to account for a more general forcing wave that encompasses the evanescent waves scattered by the other floes in the array. Matching our representations of the velocity potential in the ice-covered and free-surface fluid domains at their common boundary enabled us to retrieve the remaining unknowns and hence complete the solution process.

After validating our method through comparison to the alternative interaction theory of Peter et al. (2006) in test problems, we used a selection of numerical results to investigate the way in which the

response and scattering properties of the straight-line array change as certain quantities are varied. It was found that the angle of incidence of the incoming wave is a primary factor in producing floe interactions, so that the effects of the array will only be visible for close floe separations with a normally incident wave but will persist at large separations when there is a significant angle of incidence. The introduction of thickness variations and realistic submergence were shown to be capable of altering the response of the array to the incoming wave. However, overall behavioural changes caused by these new features were difficult to ascertain, particularly because of the complicated form of the scattering in this periodic system, in which multiple reflected waves may propagate away from the array. These waves, which exist only in certain régimes, were seen to be generated with large amplitudes when the floe spacing was tight and the wave travels in a direction nearly parallel to the array itself.

There is a natural extension to this work in which the geometry consists of a finite number of the infinite single-line arrays that we have considered herein. This would simply involve matching the solutions for adjacent single-line arrays at a common interface, where the solution for the single-line array would need to be extended to a more general incident wave in a similar manner to the way in which we modified the solution for the solitary floe for use in single-line array earlier. In this multiple-line array there would be no need for the arrays to be identical, only that they obey the same periodicity condition. This work is the topic of a separate paper.

FUNDING

This work was supported by the University of Otago and by the Marsden Fund Council from Government funding administered by the Royal Society of New Zealand [UOO308].

ACKNOWLEDGEMENTS

The authors wish to thank Dr Malte Peter for providing comparative results.

REFERENCES

Abramowitz, M and Stegun, I (1964). *Handbook of mathematical functions* Dover.

Achenbach, J, Lu, Y, and Kitahara, M (1988). "3-d reflection and transmission of sound by an array of rods," *J. Sound Vibration*, Vol 125 (3), pp 463–476.

Andrianov, A and Hermans, A (2005). "Hydroelasticity of a circular plate on water of finite or infinite depth," *J. Fluid. Struct.*, Vol 20(5), pp 719–733.

Bauer, J and Martin, S (1980). "Field observations of the bering sea ice edge properties during march 1979," *Mon. Weather Rev.*, Vol 108, pp 2045–2056.

Bennetts, L. G (2007). *Wave scattering by ice sheets of varying thickness* PhD thesis, University of Reading.

Bennetts, L. G, Biggs, N. R. T, and Porter, D (2007). "A multi-mode approximation to wave scattering by ice sheets of varying thickness," *J. Fluid Mech.*, Vol 579, pp 413–443.

Bennetts, L. G, Biggs, N. R. T, and Porter, D (2009a). "The interaction of flexural-gravity waves with periodic geometries," *Wave Motion*, Vol 46, pp 57–73.

Bennetts, L. G, Biggs, N. R. T, and Porter, D (2009b). "Wave scattering by an axisymmetric ice floe of varying thickness," *IMA J. Appl. Math.*, Vol 74, pp 273–295.

Bennetts, L. G and Squire, V. A (2008). "Wave scattering by an infinite straight-line array of axisymmetric floes," *Int. J. Offshore Polar*, Vol 18(4), pp 254–262.

Linton, C (1998). "The green's function for the two-dimensional helmholtz equation in periodic domains," *J. Engng. Math.*, Vol 33, pp 377–402.

Linton, C and Evans, D (1993). "The interaction of waves with a row of circular cylinders," *J. Fluid Mech.*, Vol 251, pp 687–708.

Linton, C, Porter, R, and Thompson, I (2007). "Scattering by a semi-infinite array and the excitation of surface waves," *SIAM J. Appl. Maths.*, Vol 67(5), pp 1233–1258.

Linton, C. M and Thompson, I (2007). "Resonant effects in scattering by periodic arrays," *Wave Motion*, Vol 44(3), pp 165–175.

Meylan, M. H (2002). "Wave response of an ice floe of arbitrary geometry," *J. Geophys. Res.*, Vol 107(C1), 3005, doi:10.1029/2000JC000713.

Meylan, M. H and Squire, V. A (1996). "Response of a circular ice floe to ocean waves," *J. Geophys. Res.*, Vol 101, pp 8869–8884.

Nicorovici, N. A, McPhedran, R. C, and Petit, R (1994). "Efficient calculation of the green's function for electromagnetic scattering by gratings," *Phys. Rev. E*, Vol 49(5), pp 4563–4577.

Peter, M. A and Meylan, M. H (2004). "Infinite depth interaction theory for arbitrary floating bodies applied to wave forcing of ice floes," *J. Fluid Mech.*, Vol 500, pp 145–167.

Peter, M. A and Meylan, M. H (2007). "Water-wave scattering by a semi-infinite periodic array of arbitrary bodies," *J. Fluid Mech.*, Vol 575, pp 473–494.

Peter, M. A, Meylan, M. H, and Chung, H (2004). "Wave scattering by a circular elastic plate in water of finite depth: a closed form solution," *Int. J. Offshore Polar*, Vol 14(2), pp 81–85.

Peter, M. A, Meylan, M. H, and Linton, C. M (2006). "Water-wave scattering by a periodic array of arbitrary bodies," *J. Fluid Mech.*, Vol 348, pp 237–256.

Porter, D and Porter, R (2004). "Approximations to wave scattering by an ice sheet of variable thickness over undulating bed topography," *J. Fluid Mech.*, Vol 509, pp 145–179.

Porter, R and Porter, D (2001). "Interaction of water waves with three-dimensional periodic topography," *J. Fluid Mech.*, Vol 434, pp 301–335.

Squire, V. A (2007). "Of ocean waves and sea-ice revisited," *Cold Reg. Sci. Technol.*, Vol 49, pp 110–133.

Thompson, I, Linton, C, and Porter, R (2008). "A new approximation method for scattering by long finite arrays," *Q. J. Mech. Appl. Math.*, Vol 61(3), pp 333–352.

Timoshenko, S and Woinowsky-Krieger, S (1959). *Theory of plates and shells.* McGraw-Hill, 2nd edition.

Wang, C, Meylan, M. H, and Porter, R (2007). "The linear wave response of a periodic array of floating elastic plates," *J. Engng. Math.*, Vol 57(1), pp 23–46.